Quarterly Report for
**October 1997 - December 1997**
**Stanford Geothermal Program**
DE-FG07-95ID13370

# Table of Contents

# 1.  MEASUREMENTS OF STEAM-WATER RELATIVE PERMEABILITY

This research project is being conducted by Dr. Cengiz Satik and Professor Roland Horne. The aim of this project is to measure experimentally relative permeability relations for steam and water flowing simultaneously in a porous medium.

## 1.1 SUMMARY

A set of relative permeability relations for simultaneous flow of steam and water in porous media have been derived from an experiment conducted under conditions that eliminate most errors associated with saturation and pressure measurements. These relations showed relative permeabilities for both steam and water phases that vary with saturation in a curvilinear fashion. The saturations in this experiment were measured by using a high resolution X-ray computer tomography (CT) scanner. In addition the pressure gradients were obtained from accurate measurements of liquid-phase pressure over regions with flat saturation profiles. These two aspects constitute a major improvement in the experimental method compared to those used in the past.

## 1.2 INTRODUCTION

Application of Darcy's law to the description of simultaneous flow of two or more phases of fluids in a porous medium requires the use of relative permeability relations (Hassler, 1944; Osoba et al., 1951; Corey, 1954; Brooks and Corey, 1964). Since being introduced by Buckingham in 1907 and used extensively by investigators in the 1930's, relative permeability has been traditionally expressed as a function of saturation principally because it was believed that it depended on the pore volume occupied by the fluids (Hassler, 1944). Whereas a great many experiments have shown this to be true, a number of other experiments have shown that relative permeability depends on several other parameters such as interfacial tension, wetting characteristics and viscosity ratios of the flowing fluids (Fulcher et al., 1983; Osoba et al., 1951). Since these parameters are expected to change with the type of fluid and porous medium, and even with temperature, it should be expected that relative permeability would change for a given set of materials and experimental conditions. In addition it is also important to define residual saturation which is the smallest saturation value for a given phase to become immobile. The curves and the residual saturations together define a complete relative permeability relation.

Relative permeability relations reported in the past have been from the two main sources: 1) Theoretical methods using either field data from well tests or production histories of the wells in producing fields, 2) Laboratory experiments performed by injecting either single or two-phase fluids through small cores or porous medium models. Relative permeability relations derived from field data have generally been obtained by matching enthalpy data (Grant, 1977; Sorey et al., 1980; Horne and Ramey, 1978). In deriving these relations the reservoir is normally treated as a porous medium. The enthalpy is then determined as a function of in-situ fluid saturations which have to be estimated from the flowing fractions. These models suffer from a number of shortcomings due to the severe assumptions used. While laboratory experiments are the most reliable method to determine relative

permeability they also suffer from limitations imposed by boundary effects caused by capillary forces. Capillarity introduces nonlinear effects on the pressure and saturation distribution of the wetting phase at the core exit. Thus experiments must be designed to eliminate these effects. Osaba et al. (1951) have given a summary of the methods used to obtain relative permeability for two-component systems that eliminate or minimize such effects and that have been used successfully in problems of oil and gas. Capillary pressure effects can be overcome by use of sufficiently long cores or by use of high injection rates (Osoba et al., 1951).

One of the earliest attempts to measure relative permeability relations for single component two-phase flow was reported by Miller (1951). In these experiments liquid propane was injected into a core. Propane was allowed to flash as it moved across the core thus creating a two-phase flow with increasing gas fraction as the fluid moved further downstream. Relative permeability relations were estimated from the application of mass and energy balance. Among the first attempts to measure steam and water saturations directly were those experiments conducted at Stanford University first by Arihara (1976) and Chen (1976), and later by Council (1979) using a capacitance probe method. In this technique, the saturation was obtained from a calibration based on the relation between the capacitance and the saturation within the core (Council, 1979). However the region over which readings were obtained was small, thus leaving doubts on the reliability of the relative permeability relations obtained. Chen et al. (1978) recommended the use of a gamma-ray densitometer for measuring saturations. Later, Verma (1986) used a gamma-ray densitometer for experiments using an artificial sand pack. Though this was an improvement over the capacitance probe, the portion of the sample accessed by the densitometer was rather small (5%). Problems with overheating of the equipment during the experiments resulted in only a small part of the relative permeability curve being investigated. In addition, fluid bypass between the core holder and the sand pack was suspected to contribute to the larger steam relative permeability obtained in the experiments.

Recently, Sanchez (1987) reported the use of average recovery time of a tracer injected with the fluid to determine the water saturation in the core. In these experiments, pressure was measured at only two points a short distance away from the either end, effectively ignoring capillary end-effects. Sanchez (1987) estimated an average water saturation representing the whole core and ignored the variations in saturation expected from the capillary end-effects at low flow rates. His results showed that relative permeabilities for steam-water and nitrogen-water were similar. As a significant improvement, Clossman and Vinegar (1988) are probably the first to report the use of X-ray CT scanner to measure water and steam saturations in porous materials. They investigated steam-water relative permeability in cores from oil fields at residual oil saturations. However, the cores they used for the experiments were rather small and flow rates were moderate. Relative permeability relations were calculated from the temperature and pressure measurements obtained at the inlet and outlet of the core. Clossman and Vinegar (1988) found that the relative permeability values for the steam phase were close to those reported by Brooks and Corey (1964) but those for the liquid phase were somewhat smaller. More recently

Piquemal (1994) has reported relative permeability relations for steam and water at $180^{\circ}C$ using methods similar to those used by Verma (1986). The porous medium was an unconsolidated material packed in a tube 25 cm long and with an internal radius of 5 cm. Pressure and temperature were measured at four points 5 cm apart along the core holder. Though Piquemal (1994) did not discuss any errors in his measurements, the experiments were subject to the same problems reported by Verma (1986) who used a similar apparatus. However, it is important to notice that the results reported by Piquemal (1994) and Verma (1986) are different. Piquemal (1994) obtained results suggesting that steam-water flows are similar to nitrogen-water while Verma (1986) observed enhanced permeability of the steam phase. Very recently we reported steam-water flow experiments where significant improvements were achieved in measuring saturations and collecting experimental data (Ambusso, 1996). These results indicated a linear relationship for steam-water relative permeability. In attempting to repeat these results, we improved significantly on the experimental apparatus. Finally, a successful experiment was conducted and steam-water relative permeability was calculated. These recent results suggest a curviliniear relationship that is different than our previous results (linear relationship).

This review shows that there is a wide range of results that have been reported, even from some which used similar experimental apparatus. The main reason for this has been the difficulty in measuring saturations accurately and using incorrect pressure gradients to compute relative permeability. The investigations reported in this paper overcame these difficulties by using the X-ray CT scanner to measure saturation accurately and by evaluating pressure gradients within the zones of constant saturation only. Because the results reported in this paper are not confirming our previous results, we plan to repeat this experiment again. In this section, we first describe the experimental apparatus and method. Then we continue with a discussion of results obtained from the experiment.

## 1.3 EXPERIMENTAL APPARATUS AND PROCEDURE

The experimental apparatus used in this experiment consisted of an injection unit, and a core holder assembly. The injection unit consisted of two furnaces to generate steam and hot water and two liquid pumps. Two voltage controllers were used to control the temperatures of the furnaces. The core holder assembly differed significantly from the one used in the experiments discussed in Satik et al. (1995) and Ambusso et al. (1996). The core holder was constructed from a plastic (ultem) tube, a high temperature epoxy and several high temperature plastic fittings. In preparing a core holder, the first step was to heat a Berea sandstone core sample in an oven at $800^{\circ}C$ overnight to deactivate clays and to get rid of residual water (Ma and Morrow, 1991). Previously, the oven temperature had been set to $400\text{-}450^{\circ}C$ (Ambusso, 1996) and serious plugging problems were encountered during the experiments using the core holders made using these cores. The problems of plugging during the flow experiments were solved by simply increasing the oven temperature from $400\text{-}450\ ^{\circ}C$ to $800^{\circ}C$. Temperatures along the core were measured by T-type thermocouples inserted at locations where pressure ports are located. There were eight pressure and temperature measurements along the core holder, two at the inlet and one at outlet. Heat losses on the core body were measured by using nine heat flux sensors

placed at various locations along the core body. All of the measurements during the experiment were taken by using a data acquisition system. Direct monitoring of pressures and temperatures during the experiment enabled us to determine when steady state conditions had been reached.

The Berea sandstone rock samples used for these experiments had the following properties; permeability 1200 md, porosity 22%, length 43.2cm and diameter 5.04 cm. After the heating to $800^{\circ}$C to deactivate clays, the core sample was epoxied in a plastic (ultem) tube leaving the two ends of the core sample free of epoxy. Following this, eight pressure ports were drilled at fixed intervals along the edge of the core holder body. The two ends of the core holder were then machined for attachment of the end plates. After mounting all of the necessary pressure fittings, the core holder was tested for leaks. Finally, heat flux sensors were placed along the core holder before it was covered with an insulation material made of ceramic blanket. The core was then placed on a motorized bench that could be moved to precise locations in the high resolution X-ray CT scanner. A picture of the experimental apparatus within the X-ray CT scanner is shown in Figure 1.1.



*Figure 1.1: A picture of the X-ray CT scanner and the core holder used in flow experiments*

The experimental procedure was as follows. First, air inside the pore space was removed by using a vacuum pump, then the core was scanned at predetermined locations to obtain dry-core CT ($CT_{dry}$) values. Next, deaerated water was injected into the core to saturate it completely. Then the core was scanned again at the same locations to obtain wet-core CT ($CT_{wet}$) values and pressure and temperature readings were again taken at this time. Steady-state relative permeability experiments involve injection of varying fractions of steam and water into the core. Measurements at each step result in a single data point on the relative permeability vs. saturation curve. Starting from a completely water saturated core and injecting steam at increasing fractions will give rise to a drainage process while the opposite procedure gives rise to an imbibition process. Each step continued until steady-state conditions at which injection and production rates became the same for both steam and water and also pressures and temperatures stabilized. At the onset of steady-state conditions, another X-ray scan was done along the core at the same locations to

obtain CT ($CT_{exp}$) values corresponding to the particular steam-water fraction. Next, the steam-water fraction was changed and the above procedure was repeated.

During the experiment, an interpretation software was used to calculate the porosity and saturation distributions from the *CT* values obtained with the scanner. To calculate porosity the following expression was used:

$$f = \frac{CT_{wet} - CT_{dry}}{CT_{water} - CT_{air}} \quad \text{............................................................................……(1.1)}$$

where $CT_{water}$, $CT_{air}$ are CT numbers for water and air, respectively. Similarly, the expression used to calculate saturations is:

$$S_{st} = \frac{CT_{wet} - CT_{exp}}{CT_{wet} - CT_{dry}} \quad \text{............................................................................(1.2)}$$

and

$$S_w = 1 - S_{st} \quad \text{............................................................................(1.3)}$$

where $S_{st}$ and $S_w$ denote steam and water saturations, respectively.

## 1.4 EXPERIMENTAL RESULTS

The single core dynamic method was used for the measurement of the relative permeability. This method required that a two-phase mixture of steam and water be injected into a core. By changing the flowing fractions of each phase and letting the system adjust itself to steady-state conditions, the relative permeability relations were determined from the knowledge of the flowing fractions and the measured pressures and temperatures. To determine the flowing fractions it was necessary that the enthalpy of the injected fluid be known accurately. Thus it was important that the injected fractions of the components in the core be known before injection and the phase change accompanying pressure drop be considered.

After assembling the core and the auxiliaries, the experiment was initiated by first determining the porosity of the core. This was done by taking X-ray CT scans of the core at various locations when it was dry and again when it was fully saturated with water. First, the core was kept under vacuum for several hours and the initial scan, referred to as the *dry scan*, was performed to obtain $CT_{dry}$ values. Following this, a steady stream of water at low flow rate (5 cc/min) for sufficiently long time (12 hours) to saturate the core completely with water. A second scan, referred to as the *wet scan*, was then conducted to obtain $CT_{wet}$ values at the same locations as the *dry scan* was performed. By using Equation 1.1 and these two sets of images obtained at every point scanned it was possible to determine the porosity distribution of the core. Figure 1.2 shows porosity images obtained at four locations along the core although we obtained a total of 42 such slices during the experiment. Average porosity profiles were also calculated by averaging porosities over each slice along the core and these are shown in Figure 1.3. Average porosity of the core was found to be about 22%. After the porosity distribution had been determined the absolute permeability was determined by flowing water at different flow

rates and measuring pressures along the core. From this test, the permeability of the core was calculated to be 1200 md.

Steady-state conditions were recognized by the stabilization of temperature and pressure. Typically stabilization took three to five hours, though some of the measurements reported here were taken after at least six hours. Once a steady state had been confirmed, the measurements of temperature and pressure were recorded together with the heat flux sensors readings. The X-ray CT scans were then taken at locations where the dry and wet scans had been taken to obtain $CT_{exp}$ values. These scans were then processed into saturation images using Equations 1.2 and 1.3. The saturation profiles presented in this paper were obtained by averaging the saturation values over a cross sectional area of the core.
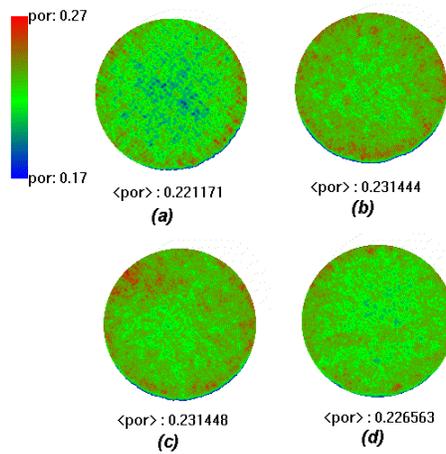


*Figure 1.2: Selected images for porosity distributions obtained from the X-ray CT scan at 1, 11, 21 and 40 cm away from the inlet of the core.*
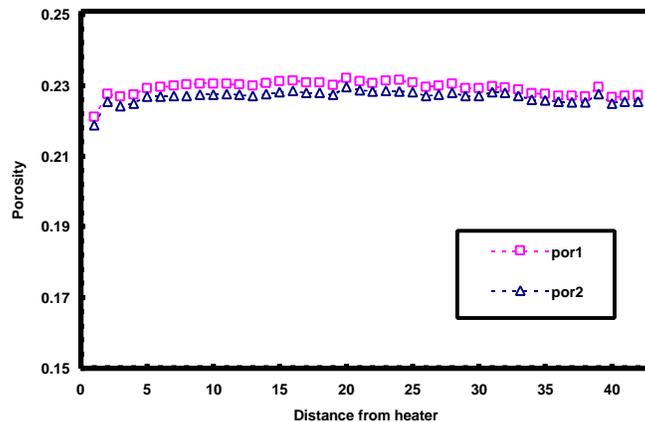


*Figure 1.3: Average porosity profiles obtained during the experiment.*

To determine whether the steam saturation distributions were in fact uniform, each image had to be examined. In general, all of the images showed very uniform saturations for most sections for all flow rates, except closer to the inlet end of the core. Figure 1.4

6

shows steam saturation distributions at four locations along the core. As shown in the first image of the figure, more water exists at the top while more steam is at the bottom of the cross-sectional area at 1 cm (Figure 1.4a). This situation existed simply because we injected the superheated steam from the bottom portion of the end plate while the hot water from the top portion. The two phases (superheated steam and subcooled water) were mixed somewhere inside porous medium. The examination of all of the 42 slices revealed that steam and hot water were fully mixed at three cm from the inlet, resulting in saturated conditions. This is also apparent from the three slices shown in Figure 1.4b, c and d.
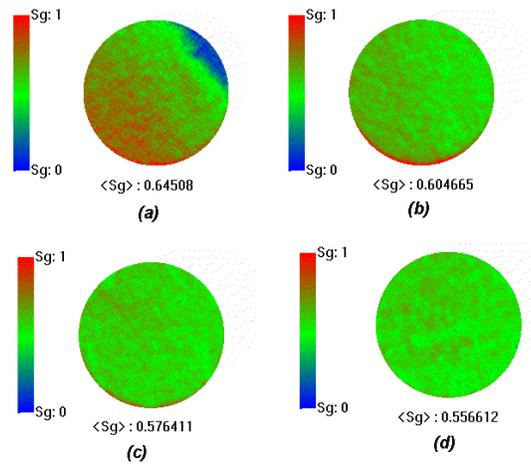


*Figure 1.4: Selected images for steam saturation distributions obtained from the X-ray CT scan at 1, 11, 21 and 40 cm away from the inlet of the core.*

During the experiment, the phase fractions of the injected fluids were changed 20 times while attempting to change the steam fraction (and steam saturation in the core). Each of these 20 steps will be referred as steps in this description (see Table 1.1). Figure 1.5 shows all of the average saturation profiles obtained during the experiments. In general all of the saturation profiles show a decreasing trend from the injection end to the production end which was also observed in the numerical simulation results for the non-adiabatic case (see Ambusso et al., 1995). As seen from all of the steps given in Figure 1.5, the values of saturation are never really constant but change gradually. Thus the flat saturation profiles are not always "flat". However the values change very little over the most of the core length and can be averaged over an interval to a representative value. The saturation profiles shown in Figure 1.5 reveal another interesting feature. The capillary end-effects are observed at low steam flow rates with high steam fraction (e.g. Steps 10 and 11).

*Table 1.1: Summary of the steps used during the experiment.*

| Step | $q_{water}$, cc/min | $q_{steam}$, cc/min | Time elapsed,min |
|------|------|------|------|
| 1 | 4.5 | 0.5 | 375 |
| 1a | 4.5 | 0.5 | 484 |
| 1b | 4.5 | 0.5 | 1071 |
| 2 | 4.5 | 0.4 | 1283 |
| 2a | 4.5 | 0.4 | 1421 |
| 3 | 4.5 | 1.0 | 1846 |
| 4 | 4.5 | 2.0 | 2047 |
| 5 | 4.5 | 2.5 | 2220 |
| 6 | 4.5 | 3.0 | 2670 |
| 7 | 4.5 | 0.8 | 2940 |
| 8 | 6.0 | 0.8 | 3035 |
| 9 | 7.5 | 0.8 | 3487 |
| 10 | 4.5 | 0.4 | 3785 |
| 11 | 4.5 | 0.3 | 3968 |
| 12 | 1.5 | 1.5 | 4217 |
| 13 | 4.0 | 0.3 | 4795 |
| 14a | 4.0 | 0.35 | 5310 |
| 14b | 4.0 | 0.35 | 5581 |
| 15 | 1.0 | 4.0 | 5733 |
| 16 | 1.0 | 1.0 | 6780 |

Figures 1.6 and 1.7 show steady-state temperature and pressure profiles, respectively. As described in the experimental apparatus section, the thermocouples were inserted through fittings for pressure taps. Thus the thermocouples made direct contact with the core sample. This was done in order to obtain the temperature measurements at the core face where the pressure readings were taken. The pressures were measured by using teflon tubes attached to the core holder body. To ensure that the readings were for the water phase these tubes were filled completely with water up to the transducers. By this method water in the tubes was assumed to be in contact with water in the core. In general all of the temperature and pressure measurements reflected the expected behavior i.e. decreasing values along the core from the injection end due to heat losses.
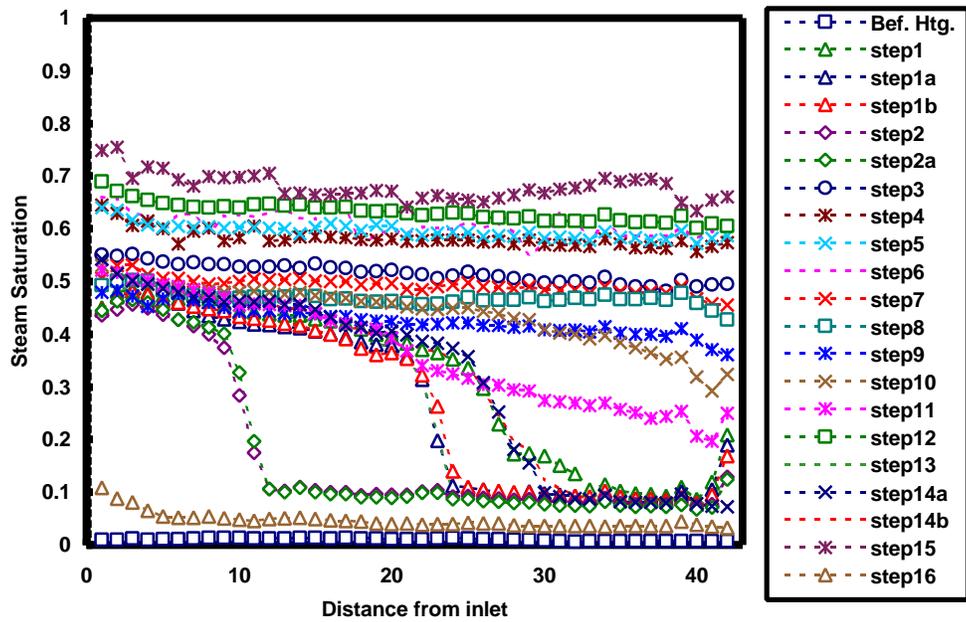
*Figure 1.5: Average steam saturation profiles for all of the steps conducted during the experiment.*
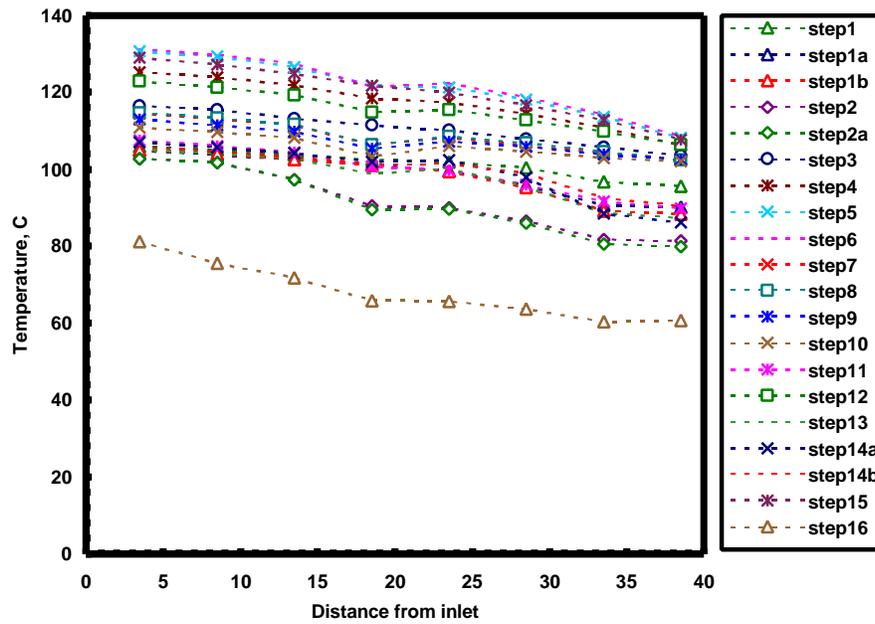


*Figure 1.6: Temperature profiles for all of the steps conducted during the experiment.*
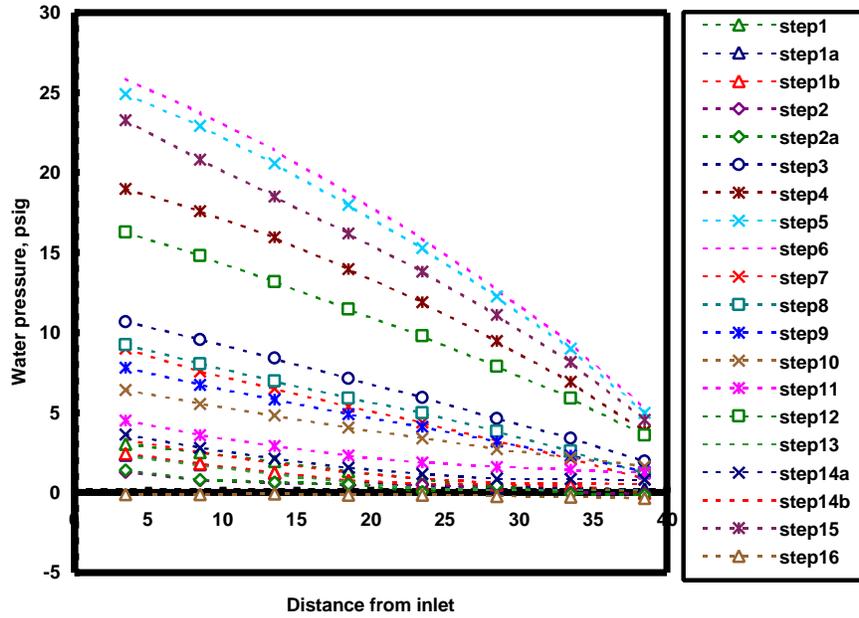
*Figure 1.7: Pressure profiles for all of the steps conducted during the experiment.*

Since it was not possible to use guard heaters, the experiments were not conducted under perfectly adiabatic conditions. Thus the interpretation of the results must take heat losses into consideration. This requires that the heat lost through the system be accounted for and the flowing fractions corrected accordingly. During the experiment, heat losses were measured only on the body of the core holder. In Figure 1.8, we show heat loss rate data collected during the experiment. Heat losses were in general very similar along the core holder body and they increased as steam fraction increased.
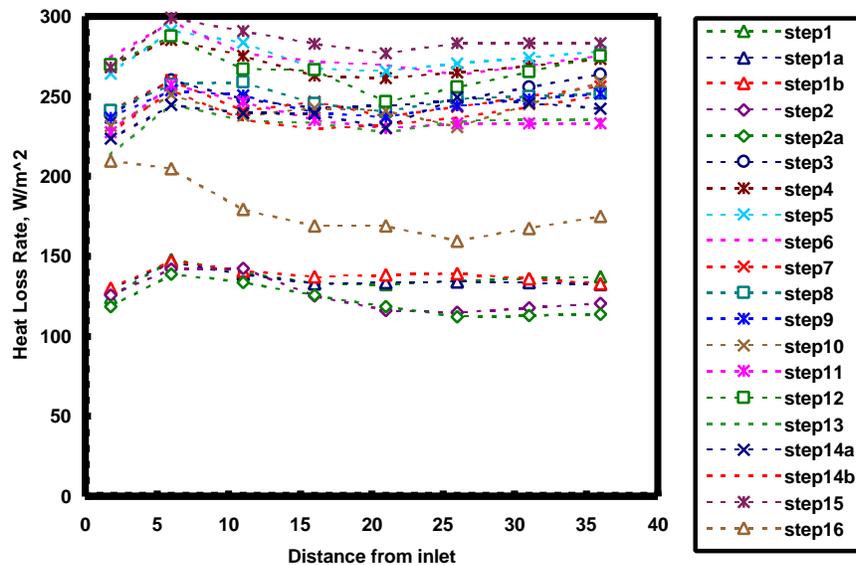


*Figure 1.8: Heat loss rate along the core holder for all of the steps conducted during the experiment.*

To calculate relative permeability we make use of the conservation equations for mass and energy fluxes:

$$m_t = m_s + m_w \quad\text{.............................................................................................................................(1.4)}$$

$$m_t h_t = m_s h_s + m_w h_w + Q \quad\text{.............................................................................................(1.5)}$$

where $m$ and $h$ refer to mass flow rate and enthalpy, respectively and the subscript $t$ refers to total, $s$ to vapor phase (steam) and w to the liquid phase (water), and $Q$ is the total heat lost at the point being considered. A schematic of the core holder is given in Figure 1.9. Using flat interface thermodynamics and mass and energy balances, the steam fraction ($X$) in the flow at any time would be given by:

$$X^1 = X^0 \frac{L_v^{\,0}}{L_v^{\,1}} + \frac{h_w^{\,0} - h_w^{\,1}}{L_v^{\,1}} - \frac{QA}{m_t L_v^{\,1}} \quad\text{.......................................................................(1.6)}$$

where $L_v$ is the latent heat of vaporization at the prevailing temperature and pressure, and A is the cross-sectional area. As demonstrated in Figure 1.9, superscripts 0 and 1 denote downstream and upstream of the point considered, respectively.
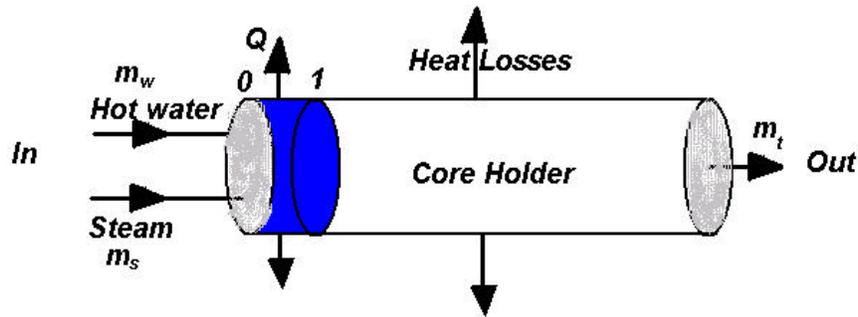


*Figure 1.9: Schematic of the core holder for relative permeability calculations..*

Then the relative permeabilities to steam and water can be calculated by using the corresponding Darcy equations for each phase in terms of the mass flow rates:

$$k_{rs} = \frac{x m_t}{r_s} \frac{\mathbf{m}_s}{kA} \frac{\Delta p}{L} \quad\text{.........................................................................................................(1.7)}$$

and

$$k_{rw} = \frac{(1-x) m_t}{r_w} \frac{\mathbf{m}_w}{kA} \frac{\Delta p}{L} \quad\text{...............................................................................................(1.8)}$$

where $k_{rs}$, $k_{rw}$ and $k$ are steam and water relative permeabilities and absolute permeability, respectively. Thus knowledge of the values of flowing mass fractions in the above equations and pressure drop along a column of the core with a constant or flat saturation provides a value for the relative permeability. Critical to the evaluation of the flowing fractions is the knowledge of the injected enthalpy and the heat losses. Figure 1.8 shows the heat losses on the core body which were computed from the measurement of the heat flux directly To determine the flowing fractions at a particular point, the heat losses at the point under consideration were evaluated (Figure 1.8) and subtracted from the total energy at the injection point. In Figure 1.10, we show the relative permeability values calculated from the experimental data and Equations 1.7 and 1.8. The relative permeability curves for the steam and water phases vary in a curvilinear fashion. Therefore these results do not agree with our previous results which suggested an "X-type" relationship (Ambusso, 1996). In Figure 1.11, we show a comparison of the steam-water relative permeability relations presented in this work to those obtained by Ambusso (1996) and Sanchez (1987). Permeability of the cores used by Ambusso (1996) and Sanchez (1987) were 600 md and 7300 md, respectively. Therefore, these results suggest a possible permeability effect on steam relative permeability. Further investigations to understand these differences are currently in progress. We plan to repeat the experiment with the same apparatus in order to confirm these recent results.
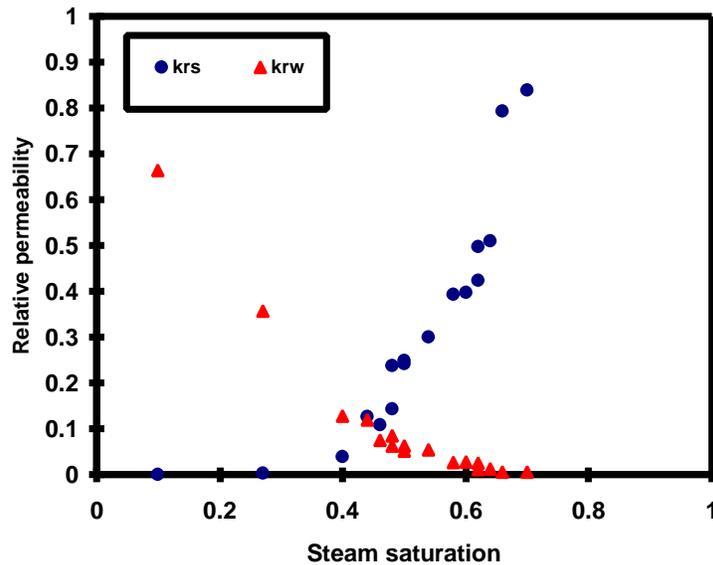


*Figure 1.10: Relative permeability for steam and water.*

## 1.5 CONCLUSION

In this section, we presented a newly measured set of steam-water relative permeability curves. A new core holder that can be used at high temperatures and pressures was designed and employed in this experiment. The core holder proved capable of withstanding the extreme conditions for the duration of the experiment. A new data acquisition system was also used to collect data and to monitor the experiment.
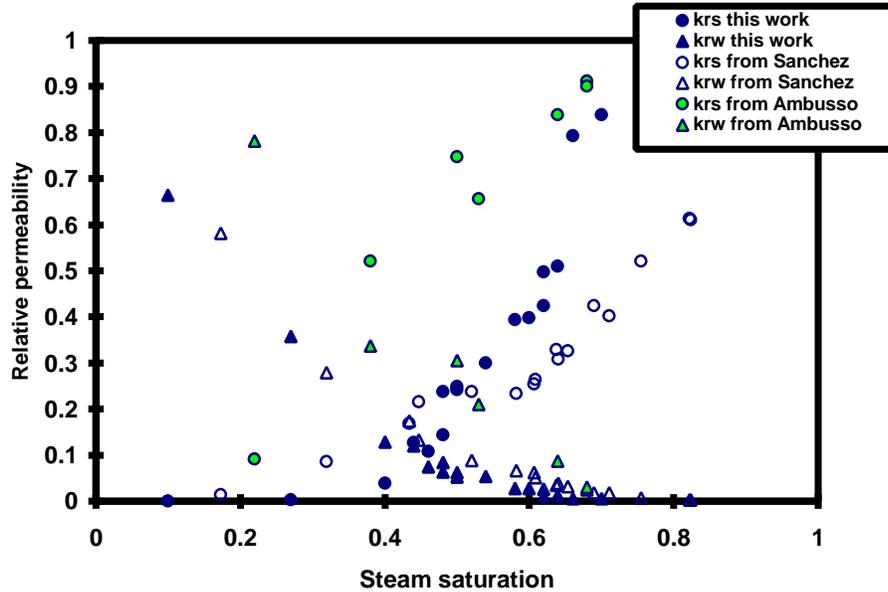
*Figure 1.11: Comparison of steam-water relative permeability curves.*

The results indicated that steam-water relative permeability vary in a curvilinear fashion with saturation as opposed to our previous results showing an "X-Type" relationship (Ambusso, 1996). However, the comparison of the results from this work to those obtained by Ambusso (1996) and Sanchez (1987) suggest an effect of permeability on relative permeability. The residual limits for both steam and water phases were not precisely defined in the experiment, because it was not possible to maintain steam quality at 100% or at a very low value due to condensation in the core. However these end points were inferred from the relative permeability curves and are about 30% for the water and less than 10% for the steam phase.

## 2. EXPERIMENTAL STUDY OF BOILING IN POROUS MEDIA

This research project is being conducted by Dr. Cengiz Satik. The objective of this study is to improve our understanding of the process of boiling in porous media by using both experimental and numerical methods. In earlier quarters we conducted a series of experiments, in both vertical and horizontal situations. These results are being used to infer relative permeability and capillary pressure, as described in Section 3 of this report. During the current quarter no additional experiments were performed, as the existing results were under investigation for the data matching project.

# 3. INFERRING RELATIVE PERMEABILITY FROM DYNAMIC BOILING EXPERIMENTS

This project is being conducted by Research Assistant Marilou Guerrero, with Dr. Cengiz Satik and Prof. Roland Horne with the cooperation of Stefan Finsterle of LBNL. The objective is to estimate relative permeability and capillary pressure by matching the measurements from a transient experiment to the results of a numerical simulation. The numerical model was constructed in TOUGH2 to simulate results taken from a vertical boiling experiment. Residual water saturation, $S_{wi}$, residual steam saturation, $S_{gi}$, pores size distribution index, $\lambda$, and gas entry pressure, $p_e$, were estimated for a Berea sandstone core by forward and inverse calculation using the Brooks-Corey relative permeability and capillary pressure functions.

## 3.1 INTRODUCTION

Recently, significant improvements were achieved in measuring saturations in steam-water relative permeability experiments (Ambusso, 1996). These results indicated a linear relationship for steam-water relative permeability. In attempting to repeat these results, Satik (1998) made improvements in the design of the experimental apparatus. A successful experiment was conducted and steam-water relative permeability was calculated as described in Section 1 of this report. These recent results suggest a curvilinear relationship that is different from the results obtained by Ambusso (linear relationship).

This project is taking a second approach to estimating the relative permeability by matching data from a boiling experiment with results obtained from numerical simulation. This method provides an independent way to examine the validity of the relative permeability measurements taken from previous experiments as well as to estimate capillary pressure since the parameters in the relative permeability and capillary functions used (Brooks-Corey) are interrelated.

## 3.2 EXPERIMENTAL APPARATUS

In the boiling experiment (Fig. 3.1), a 49.5 cm long Berea sandstone core with radius 25.4 cm was sealed with epoxy and insulated with ceramic fiber blanket. The core was first saturated with liquid water and then heated at the bottom. Water was allowed to flow from the top end of the core, which was maintained at atmospheric conditions. The heater was insulated to reduce heat loss. During the 169.5 hour vertical boiling experiment, temperature, water pressure, and steam saturation were measured at 41 points along the length of the core. The power level was increased nine times from 0.864 mJ/sec to 10.42 J/sec. A detailed description of this experiment was included in the last quarterly report, and can be found in Satik (1997). Table 3.1 shows the properties of the sandstone and materials used in the experiment.
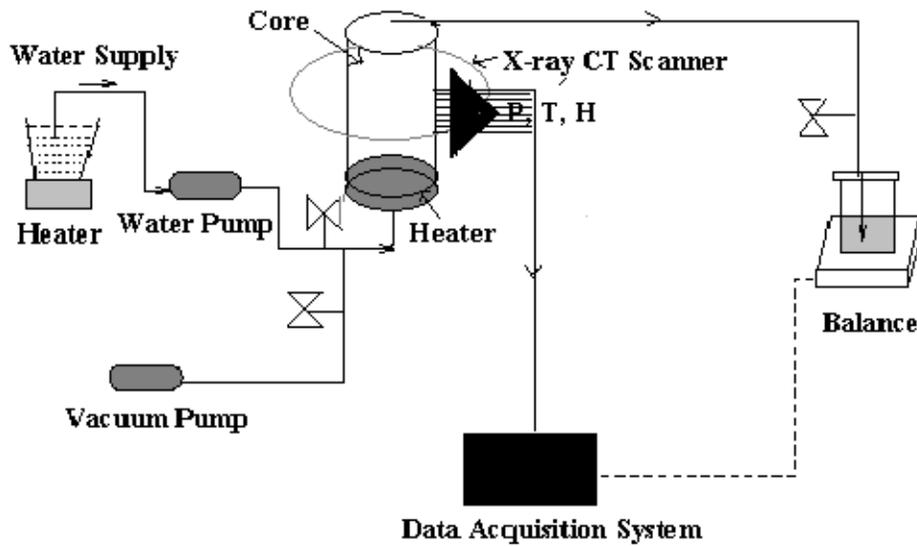
*Figure 3.1. Schematic diagram of the experimental apparatus (from Satik, 1997).*

*Table 3.1. Properties of the materials used in the boiling experiment.*

| Material | $\rho$ kg/m$^3$ | k $10^{-13}$ m$^2$ | $\phi$ % | $\alpha$ W/m-$^0$C | C J/kg-$^0$C |
|---|---|---|---|---|---|
| Berea | 2163 | 8.487 | 22 | 4.326 | 858.2 |
| Heater | 2200 | | | 2.885 | |
| Heater insul. | 529 | | | 0.125 | 1046.6 |
| Epoxy | 1200 | | | 0.577 | 1046.6 |
| Insulator | 192 | | | 0.090 | 104.7 |

### 3.3 MODELING WITH *ITOUGH2*

TOUGH2 is a multidimensional numerical model for simulating the transport of water, steam, air, and heat in porous and fractured media (Pruess, 1991). A second program ITOUGH2 provides inverse modeling capabilities for the TOUGH2 codes and solves the inverse problem by automatic model calibration based on the maximum likelihood approach (Finsterle et al., 1996). In this study, parameters were estimated based on temperature, water pressure, steam saturation, and heat flux for which a corresponding TOUGH2 output was already available, including initial guesses for the parameters to be estimated.

### Grid

The TOUGH2 simulation grid used is a two-dimensional radial model with 3 rings and 51 layers (Fig. 2). Except for layers 46-51 (six bottommost layers), the first (innermost) ring represents the core; the second ring represents the epoxy; and the third ring represents the

insulator. The heater is in layer 46, ring 1; while the heater insulator is in layers 47-51, rings 1-3. Rings 2-3 in layer 46 consist of epoxy and core insulator, respectively. Constant pressure boundary conditions are applied to layer 1 (topmost layer) in ring 1; while ambient conditions are applied to layer 1 in ring 2. To simulate a constant pressure boundary and ambient conditions, layer 1 - rings 1-2 are given a much larger volume than the core layers. Since there is no fluid flow in the radial direction, permeability values that allow flow are assigned only in the angular and vertical directions.
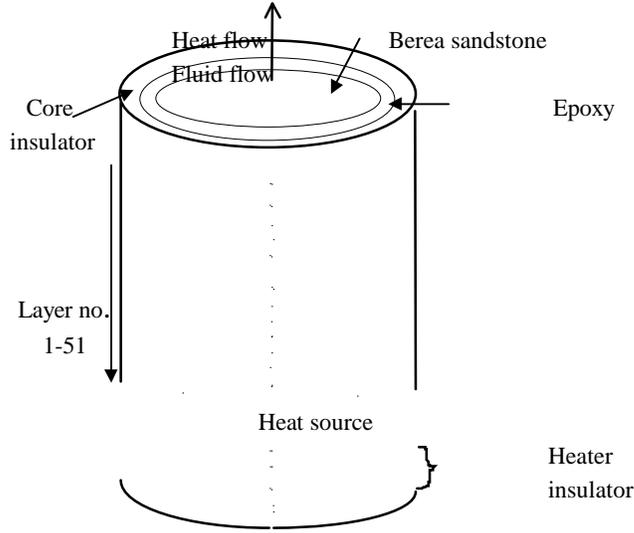


*Figure 3.2.     Schematic diagram of the 3×51 TOUGH2  model.*

## 3.4 BROOKS-COREY FUNCTIONS

The Brooks-Corey relative permeability functions are given as:

$$k_{rl} = S_{ek}^{(2-3l)/l} \quad ........\text{…………………….................................................(3.1)}$$

$$k_{rg} = (1 - S_{ek})^2 (1 - S_{ek}^{(2-3l)/l}) \quad ...\text{…………………….......…..........(3.2)}$$

The Brooks-Corey capillary pressure functions are given as

$$p_c = -p_e \left[ e / \left( 1 - S_{lrc} \right) \right]^{-1/l}$$
$$\quad - \left( p_e / l \right) \left[ e / \left( 1 - S_{lrc} \right)^{(1-l)/l} \right] \left( S_l - S_{lrc} - e \right) \qquad \text{for } S_l < (S_{lrc} - e) \text{…....(3.3)}$$

$$p_c = p_e (S_{ek})^{(2-3l)/l} \qquad\qquad\qquad \text{for } S_l \geq (S_{lrc} - e) \text{……...(3.4)}$$

where

$$S_{ec} = (S_l - S_{lrc}) / (1 - S_{lrc}) \text{...............……………………….........(3.5)}$$

$$S_{ek} = (S_l - S_{lrk}) / (1 - S_{lrk} - S_{gr}) \text{.......……......…………………………….(3.6)}$$

and $S_l$ is the liquid saturation; $S_{lrk}$ is the residual liquid saturation in the relative permeability function; $S_{gr}$ is the residual gas saturation; $S_{lrc}$ is the residual liquid saturation in the capillary pressure function; $\lambda$ is the pore size distribution index; and $p_e$ is the gas entry pressure.

## 3.5 PARAMETER ESTIMATION

### Forward Calculation

To avoid time-consuming inverse calculations, forward runs were done first to roughly match the experimental data in terms of temperature, pressure, and steam saturation with simulated results. The sensitivity of the system response to the different parameters under investigation ($S_{wi}$, $S_{gi}$, $\lambda$, and $P_e$) was determined by changing the parameters one at a time. However, since these parameters are sensitive only under two-phase condition, the system response as calculated by TOUGH2 changed only when there were steam and water present. Thus, significant changes in system response was observed only in the latter part of the history.

Results of the sensitivity analysis showed that two-phase behavior was observed at an earlier time at lower values of $S_{wi}$, where the core was more water-filled. Conversely, two-phase behavior was observed at a later time at a higher $S_{wi}$, where the core was more steam-filled. The capillary pressure decreased as $S_{wi}$ was increased

Boiling occurred earlier at lower $S_{gi}$, while it occurred later at higher $S_{gi}$. The core was more water-wet at higher $S_{gi}$ than at lower $S_{gi}$. The capillary pressure at $S_{wi}$ was not affected since it is not a function of $S_{gi}$ at all.

At lower values of $\lambda$, two-phase behavior was observed at a later time than at higher values of $\lambda$. The relative permeability of water became more concave upwards at lower $\lambda$, then became linear at a certain value, after which it became more concave downwards. The capillary pressure increased as $\lambda$ was decreased.

Furthermore, two-phase conditions occurred earlier as $p_e$ was decreased. This was due to the lower capillary pressure required to displace the water by steam.

Since the Brooks-Corey capillary function is greatly dependent on $\varepsilon$, the effect of this parameter on the system response was also studied. Increasing $\varepsilon$ decreased the capillary pressure, thereby allowing two-phase condition to occur at an earlier time. In addition, the plateau at the maximum capillary pressure is wider at higher values of $\varepsilon$.

By trial-and-error the best fit was obtained at the following values: $S_{wi}$=0.3, $S_{gi}$=0.125, $\lambda$=0.45, $p_e$=660 Pa, and $\varepsilon$ =0.1. The measured and simulated temperature data more closely matched at later times, particularly under two-phase conditions (Fig. 3.3). The

greatest temperature differences between experimental and simulated data are observed at early time, and these are by as much as 18°C. On the other hand, the measured and calculated pressure data do not match as closely as the temperature data, although the first data points at the last two time measurements coincide (Fig. 3.4). The greatest difference between the experimental and calculated pressure values is 5516 Pa (0.8 psi). The observed and simulated steam saturation data give a satisfactory match in that the calculated data mimic the trend of the experimental data (Fig. 3.5). The maximum difference between measured and simulated data is 0.2, and this is observed in early time. Incidentally, the steam and water relative permeability values match closely the measured relative permeability obtained by Ambusso (1996) (Fig.3.6). The corresponding Brooks-Corey capillary pressure curve is shown in Fig. 3.6.
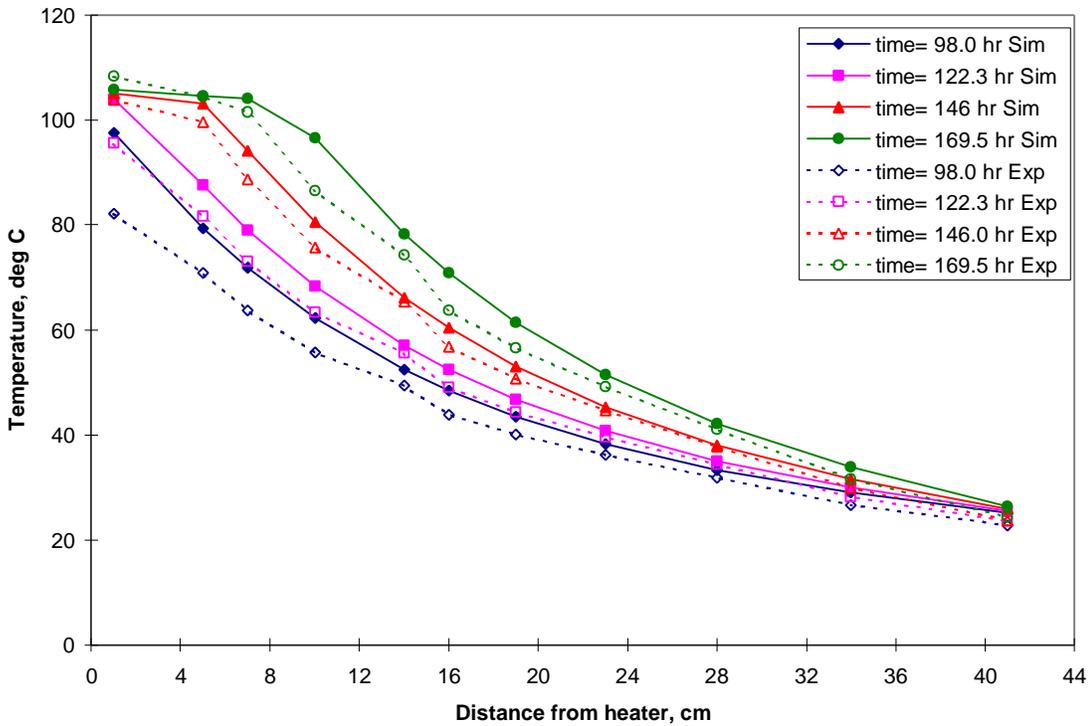


*Figure 3.3.    Comparison of observed and simulated temperature data based on forward calculations.*
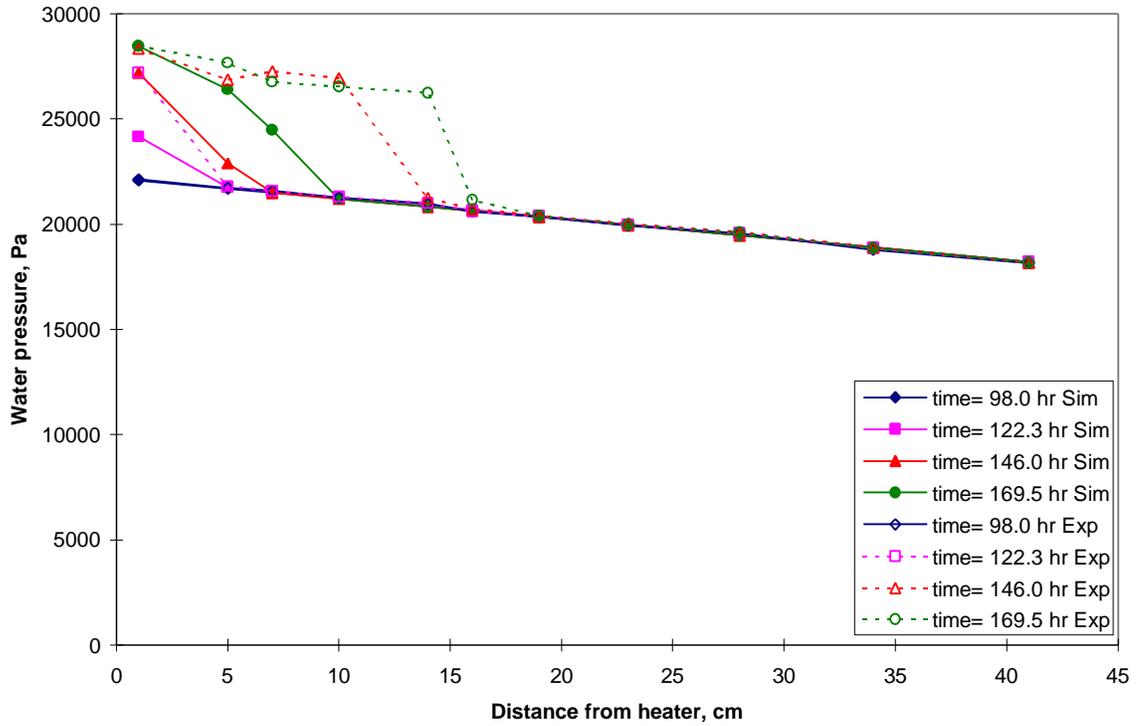
*Figure 3.4.    Comparison of observed and simulated pressure data based on forward calculations.*
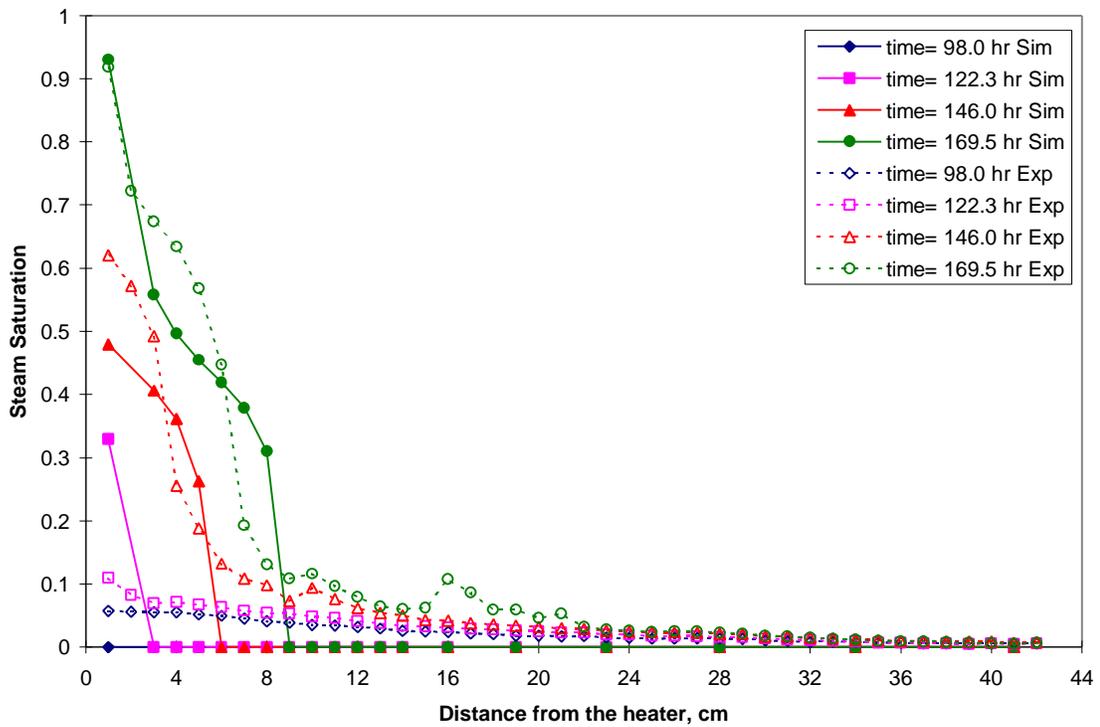


*Figure 3.5.    Comparison of observed and simulated steam saturation   data based on forward calculations.*

**Inverse Calculation**

The inverse calculation was divided into two parts: from day 0 to day 5.13, during which the system was under single-phase conditions; and from day 5.13 to day 7.06 during which the system was under two-phase conditions. This was done to separate the parameters that are sensitive to temperature, pressure, and steam saturation only under certain conditions (i.e. single-phase or two-phase conditions).

Using single-phase data, the sensitivity of the thermal conductivity of the sandstone, $\alpha_s$, thermal conductivity of the heater insulator or simply base, $\alpha_b$, thermal conductivity of the core insulator, $\alpha_i$, and the thermal conductivity of the heater, $\alpha_h$ were determined. The parameter standard deviations used were as follows: $\sigma_{\alpha s}=0.2$ W/m-$^o$C, $\sigma_{\alpha b}=0.02$ W/m-$^o$C, $\sigma_{\alpha i}=0.05$ W/m-$^o$C, and $\sigma_{\alpha \eta}=0.02$ W/m-$^o$C. Taking the thermal conductivity parameters three at a time, $\alpha_h$ came out as the least sensitive parameter among those being considered in the analysis, where the sensitivity coefficient was the indicator used. Thus, it was decided that the three other thermal conductivity parameters would be employed in the inverse calculations. The other parameters studied were porosity and absolute permeability of the sandstone. However, the estimated porosity value obtained from the inverse calculation was too large at 0.41 (compared to the measured porosity value of 0.22), hence it was discarded. On the other hand, the absolute permeability is not a sensitive parameter at all.
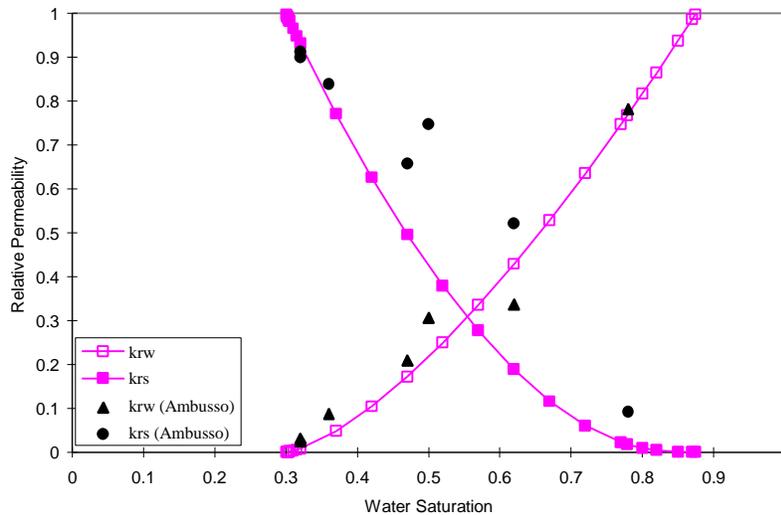


*Figure 3.6. Brooks-Corey relative permeability curves at $S_{wi}=0.3$, $S_{gi}=0.125$, and $\lambda=0.45$. The measured relative permeability values from Ambusso (1996) are shown for comparison.*
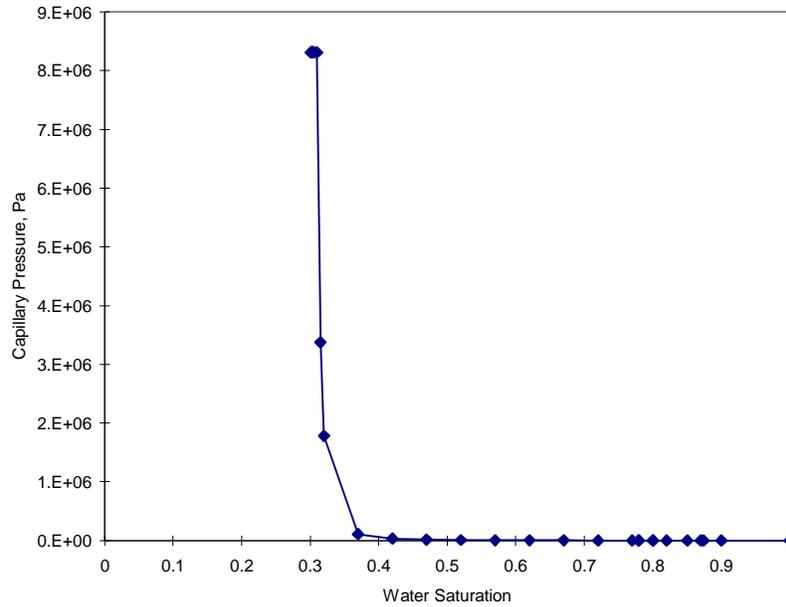
*Figure 3.7. Brooks-Corey capillary pressure curve at $S_{wi}=0.3$, $S_{gi}=0.125$, $l=0.45$, $P_e=660$ Pa and $e=0.1$.*

Results of the inverse calculation using single-phase data showed that the estimated thermal conductivity parameters considered gave a good match between the observed and calculated data at early time. They were held fixed in the second part of the inverse calculation (using two-phase data) to estimate $S_{wi}$, $S_{gi}$, $\lambda$, and $p_e$. Surprisingly, the simulated system response only gave a close fit at late time (two-phase conditions) and distorted the match made earlier in the first part of the calculation.

To eliminate the problems encountered earlier in the inverse calculation, only two-phase data were used in the succeeding calculations. Using these data, the calculation was again divided into two parts. The first part involved estimation of $\alpha_s$, $\alpha_b$, and $\alpha_i$ employing the same values for standard deviations, $\sigma_{\alpha s}$, $\sigma_{\alpha b}$, and $\sigma_{\alpha i}$. The resulting estimates from ten ITOUGH2 iterations ($\alpha_s=4.382$ W/m-C, $\alpha_b=0.038$ W/m-C and $\alpha_i=0.118$ W/m-C) gave a very good fit in terms of temperature. At this point, the standard deviation of the pressure and steam saturation data had not been reduced yet. The squares of the standard deviation constitute the diagonal elements of the *a priori* covariance matrix, whose inverse is used to weight the fitting error and scale the observation data (Finsterle, 1997).

In the second part of the inverse calculation using two-phase data, the standard deviation values of the pressure and steam saturation data were reduced to 1 psi (6895 Pa) and 0.1, respectively from their former values of 13790 Pa (2 psi) and 0.2. Fixing the thermal conductivity parameters (using the estimated values), the estimated relative permeability and capillary pressure functions parameters are as follows: $S_{wi}=0.176$, $S_{gi}=0.170$, $\lambda=0.47$, and $p_e=217$ Pa.
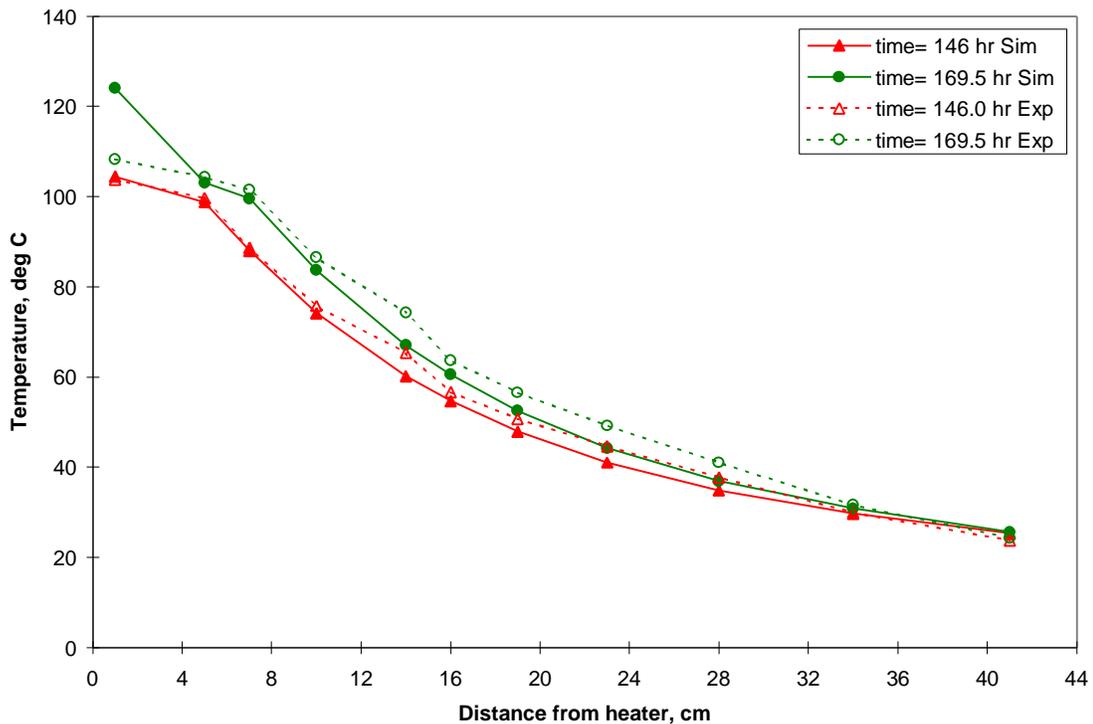
*Figure 3.8. Comparison of observed and simulated two-phase temperature data based on inverse calculations.*

Apart from the temperature data in the first 4 cm (from the heater), the observed and simulated data definitely have a better fit than the ones calculated from the initial guesses (obtained from the forward run) (Fig 3.3 and Fig. 3.8). Similarly, the fit of the steam saturation data is improved by using the estimated values (Fig. 3.5 and Fig. 3.10). Although the maximum calculated steam saturation at any given time is slightly greater than the maximum experimental value, most of the data points in the two-phase region match. On the other hand, the fit of the pressure data is worse using the estimated values than using the initial guesses (Fig. 3.4 and Fig. 3.9). This can perhaps be improved by using another scaling factor. Table 3.2 summarizes the initial guesses and estimated values.

The resulting relative permeability curves cover a wider range of water saturations since the decrease in $S_{wi}$ is greater than the increase in $S_{gi}$ (Fig. 3.11). The relative permeability of water is almost linear while $k_{rs}$ has the same shape as in Fig. 3.6. The relative permeability curves appear to be shifted to the left of Ambusso's curves. Moreover, the capillary pressure is lower than the initial guesses (Fig. 3.12).
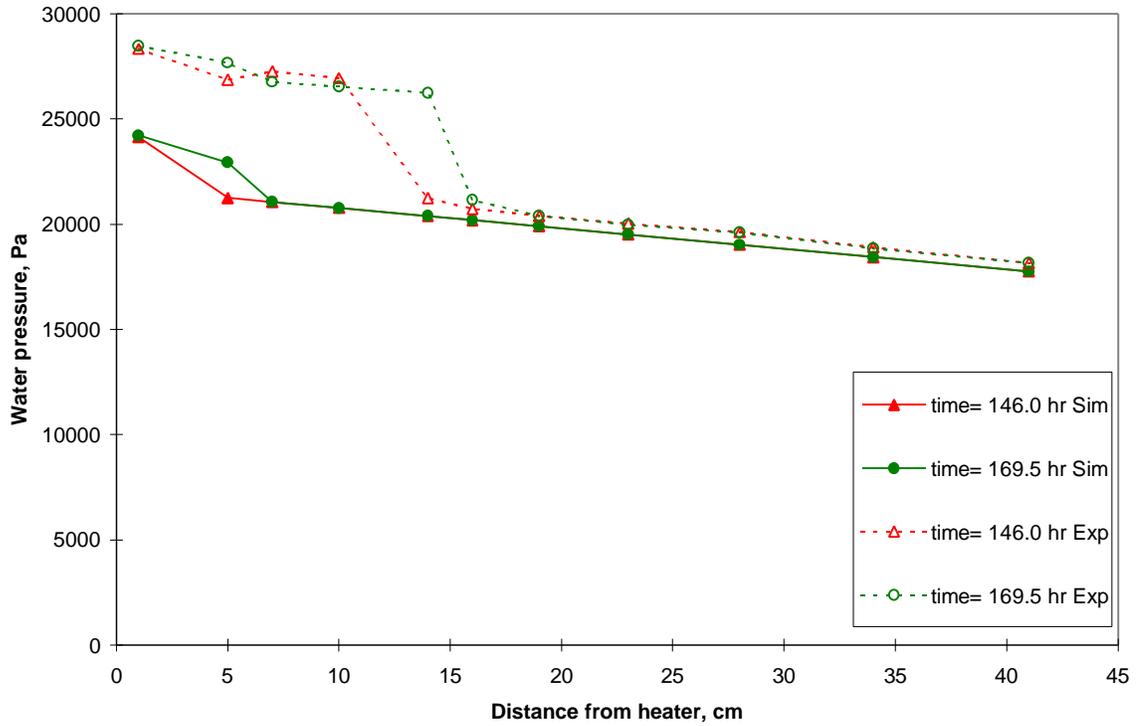
*Figure 3.9. Comparison of observed and simulated two-phase pressure data based on inverse calculations.*
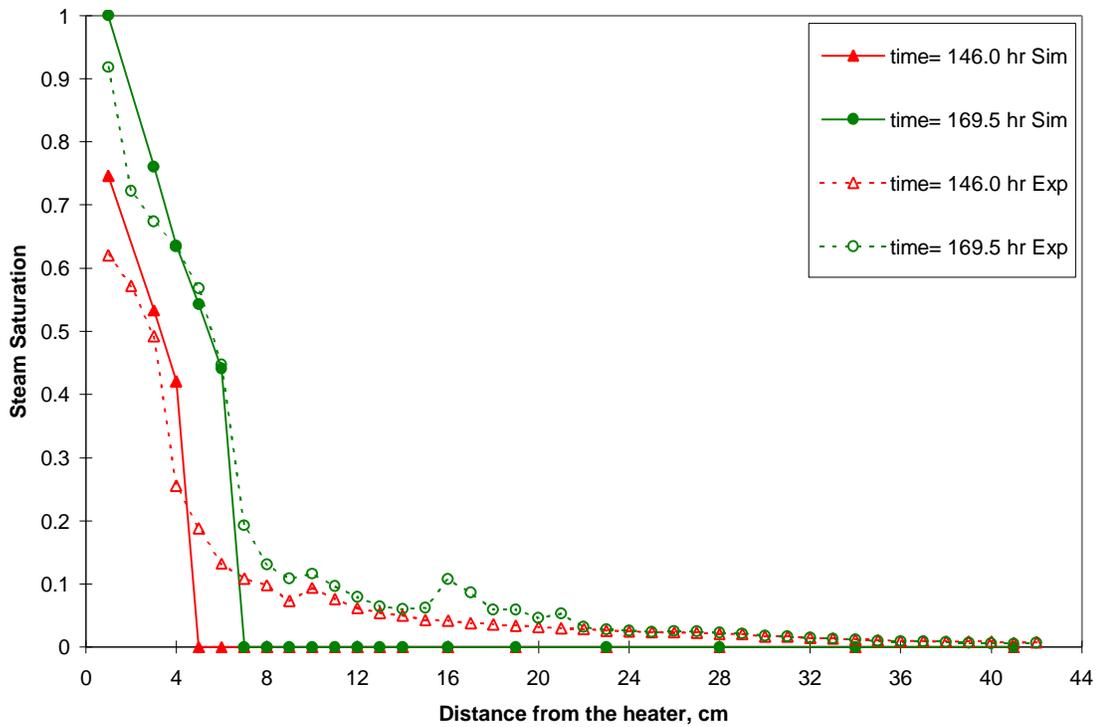


*Figure 3.10. Comparison of observed and simulated two-phase steam saturation data based on inverse calculations.*

24

## 3.6 CONCLUSION

It has been demonstrated that it is possible to infer relative permeability using transient experimental data by inverse calculation. To improve the fit, further study using two-phase data will be performed. Also, single-phase data will be used in forward calculations to verify the validity of the estimates using two-phase data.
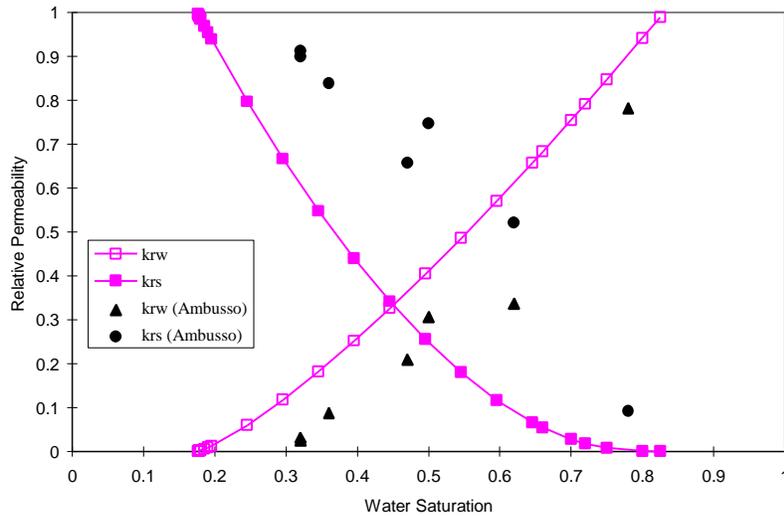


*Figure 3.11. Brooks-Corey relative permeability curves at $S_{wi}=0.176$, $S_{gi}=0.170$, and $\lambda=0.47$.*
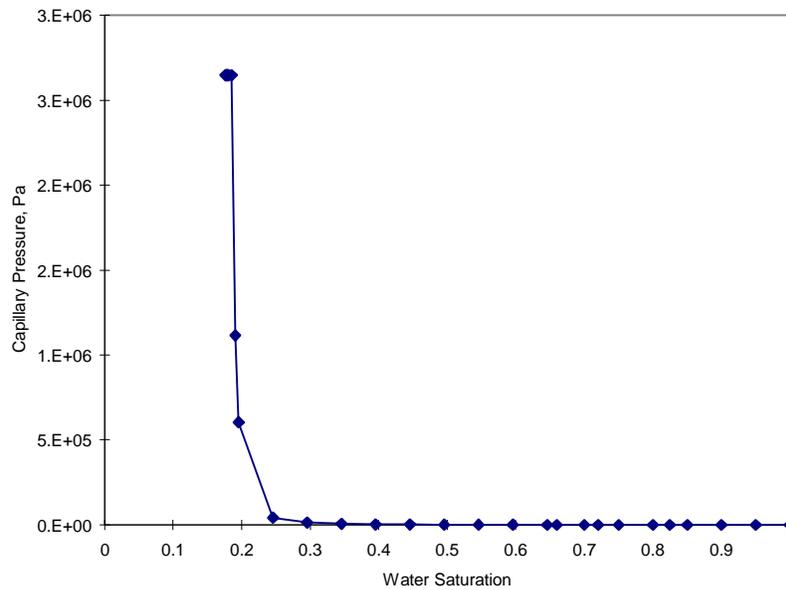


*Figure 3.12. Brooks-Corey relative permeability curves at $S_{wi}=0.176$, $S_{gi}=0.170$, $\lambda=0.47$, $P_e=217.3$ Pa, and $\epsilon=0.01$.*

*Table 3.2. Summary of initial guesses and estimated values of the parameters studied.*

| Parameter | Initial guess | Estimate | Difference |
|---|---|---|---|
| $\alpha_s$ | 4.326 | 4.382 | 0.056 |
| $\alpha_b$ | 0.125 | 0.038 | -0.087 |
| $\alpha_i$ | 0.090 | 0.118 | 0.028 |
| $S_{wi}$ | 0.300 | 0.176 | -0.173 |
| $S_{gi}$ | 0.125 | 0.170 | 0.045 |
| $\lambda$ | 0.45 | 0.47 | 0.02 |
| $p_e$ | 660.0 | 217.3 | -442.7 |

# 4. APPLICATION OF X-RAY CT IN POROSITY AND SATURATION MEASUREMENT

This project is being conducted by Research Assistant Meiqing He, Dr. Cengiz Satik and Professor Roland Horne. The aim of this project is to identify and to characterize fractures existing in geothermal rocks using X-ray computer tomography (CT). The porosity and saturation calculation processes are closely related to fracture calibration. In earlier reports, we discussed the fundamental physics of the CT technique and proposed two ways of porosity and saturation calculation. We also proposed a denoising method, soft-thresholding the coefficients of the wavelet transform. In this report we present the application of soft-thresholding to CT images of Geysers' core, propose a fracture aperture characterization method and discuss issues related to the characterization processes.

## 4.1 THEORETICAL DISCUSSION

### 4.1.1 Soft-thresholding in core image denoising

The soft-thresholding algorithm was introduced in the last quarterly report along with an example of one-dimensional signal denoising. This denoising procedure comprises three steps, (1) forward wavelet transform, (2) wavelet coefficients thresholding and (3) inverse wavelet transform. In the two-dimensional case, we apply a high-pass filter and low-pass filter on the rows and columns of the image data respectively. After one level decomposition, we obtain the following pattern shown in Figure 4.1.

| LL | LH |
|----|----|
| HL | HH |

*Figure 4.1 Coefficients pattern after one level of wavelet decomposition.*

The noise level $\sigma$ is estimated from the median value of detail subimage HH. We also know that white noise is proportional to $\log \sqrt{N}$, where N is the signal length. For the two-dimensional core image the threshold is chosen as $\sigma \log N$, where N usually is the dimension of image, 512.

### 4.1.2 Fracture extraction using gradient operator based on calibration data

From the line profile of core CT number we can tell the existence of a fracture by the valleys in the profile. In the two-dimensional density image, a fracture is shown as a dark region. In Figure 4.2(a), four main fractures can be identified as valleys. Commonly the gaps are filled with air. Note that the CT numbers inside the gaps do not give the typical CT number of air, which is -1024, as we expect. Instead, the CT numbers in the valleys indicate values around 1700. This is an effect often referred to as dispersion of the CT response, which is caused by the finite beam width and oversampling. Usually an infinitesimal point can appear within four to nine voxels surrounding the voxel in which

the point is located. Also if the voxel contains more than one component, the resulting attenuation response is determined by the volume fraction of each component and the attenuation response for each pure component. The integrated missing mass (CT number) corresponds to the gap size linearly. Thus a general approach is to run a calibration using homogeneous material with an artificial fracture. The fracture aperture is calibrated before being scanned in the CT scanner. The correlation between the integrated CT number over the gap and the calibrated aperture can be obtained using line fitting. With this preknowledge, we can deal with aperture characterization of natural fractures. However we need to identify the starting and ending point of the integration. Edge detection will allow us to mark the boundary of the integration.

We tried to use the Roberts gradient operator (Pratt, 1991) to detect edges. The impulse response arrays for the 3x3 orthogonal differential Roberts operator area as follows:

*Row Gradient*    *Column Gradient*

$$\begin{bmatrix} 0 & 0 & -1 \\ 0 & 1 & 0 \\ 0 & 0 & 0 \end{bmatrix} \qquad \begin{bmatrix} -1 & 0 & 0 \\ 0 & 1 & 0 \\ 0 & 0 & 0 \end{bmatrix}$$

The advantage of the Roberts operator is its simplicity. However this method is sensitive to noise. We will see this characteristic from our experiment.
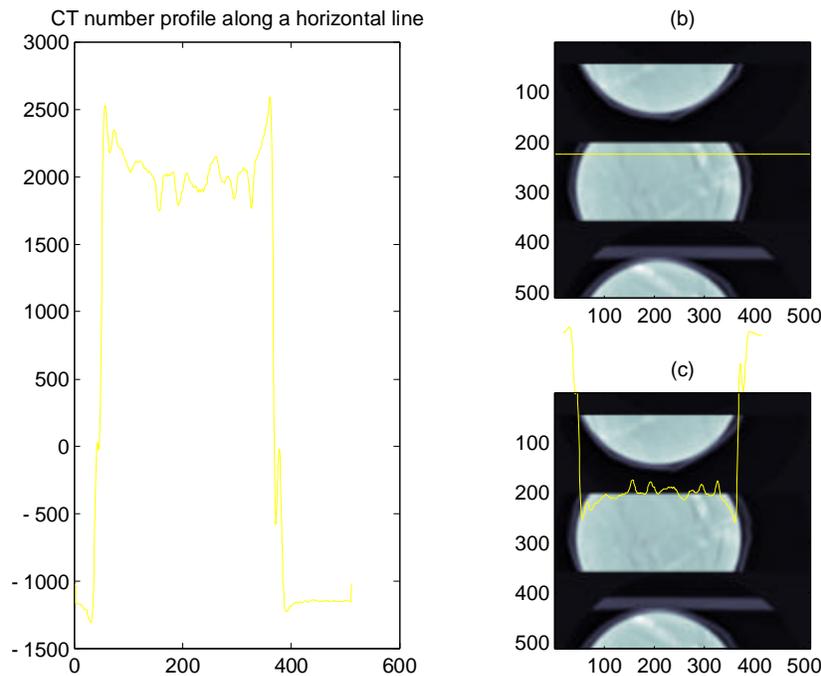


*Figure 4.2: (a) CT number profile along the 225$^{th}$ row in the image matrix. (b) Position of the profile line. (c) CT number profile vs. fractures in the core image.*

## 4.1.3 Image segmentation

The purpose of image segmentation is to recognize the feature distribution through classification. The method we tried here is called the clustering segmentation method

(Pratt, 1991). The basic assumption is that each pixel only belongs to one region (or class). The measurement vector is established on the most representative features of region. In our case, the density value is an appropriate property of a region. The segmentation process includes four steps:

[1] Making an initial guess for the density value (center) for each region.

[2] Examining each pixel. If a pixel is closer to one region than to others, the pixel is assigned a segment label.

[3] Updating the center value of each region after each iteration, because those centers change when a new member comes in.

[4] Exiting the iteration if the centers become stable.

This method is simple, but requires preknowledge of the contents of the image. The time required for iteration can be long under certain circumstances. For instance, if the image content itself is ambiguous or the initial guess for the center value is not reasonable, we need more iterations to obtain a stable center value for each region.

## 4.2 RESULTS

### 4.2.1 Denoising and edge detection

Figure 4.3(c) demonstrates the denoised core image. The difference between images in part (a) and (c) becomes obvious when we apply the Roberts gradient operator on both the original and denoised core images. Figure 4.3(b) and Figure 4.3(d) demonstrate edges detected from the original image and the denoised image. On both images, the detected fractures are marked with black dots. We can observe that these edges become disconnected. The irregular edge points are usually caused by random noise associated with photon scattering. Because the Roberts gradient operator is sensitive to noise, we will expect that Figure 4.3(b) shows more erroneous edges than Figure 4.3(d). This is evident from comparison of Figure 4.3(b) and (d). Hence the denoising method (soft-thresholding using wavelet transform) is effective indeed.

### 4.2.2 Core image segmentation

From the observation of the core image, we decided that in order to represent the whole image contents, air-filled fracture, mineral-filled fracture, outer circular region effected by beam hardening, core mounting part and core matrix, five or more regions are necessary. Results from five-region and nine-region segmentation provided knowledge about the intensity distribution over the image. Figure 4.4 demonstrates the segmentation results. In five-region segmentation, only two main mineral veins inside the core stand out as a group. Obviously, the core mounting requires more regions to characterize it. In the nine-region segmentation, the fractures are distinguishable. Although this method is not good at determining fracture aperture, it is an easy way to know the property distribution in the image. For instance, if we apply this method to a saturation image, the saturation distribution can be visualized.
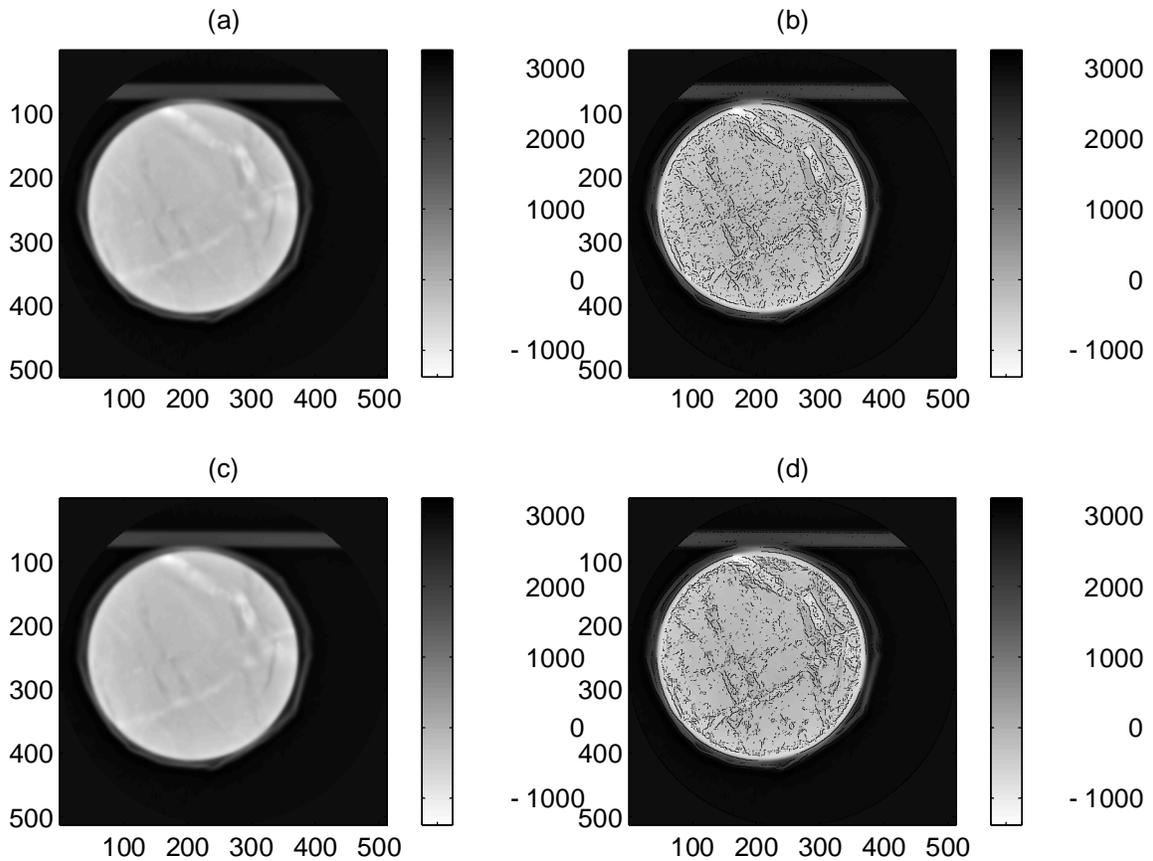
*Figure 4.3: (a) Original core image. (b) Fracture detection using Roberts gradient operator (thr=20) on original image. (c) Core image after denoising. (d) Fracture detection using Robert gradient operator (thr=20) on denoised image*
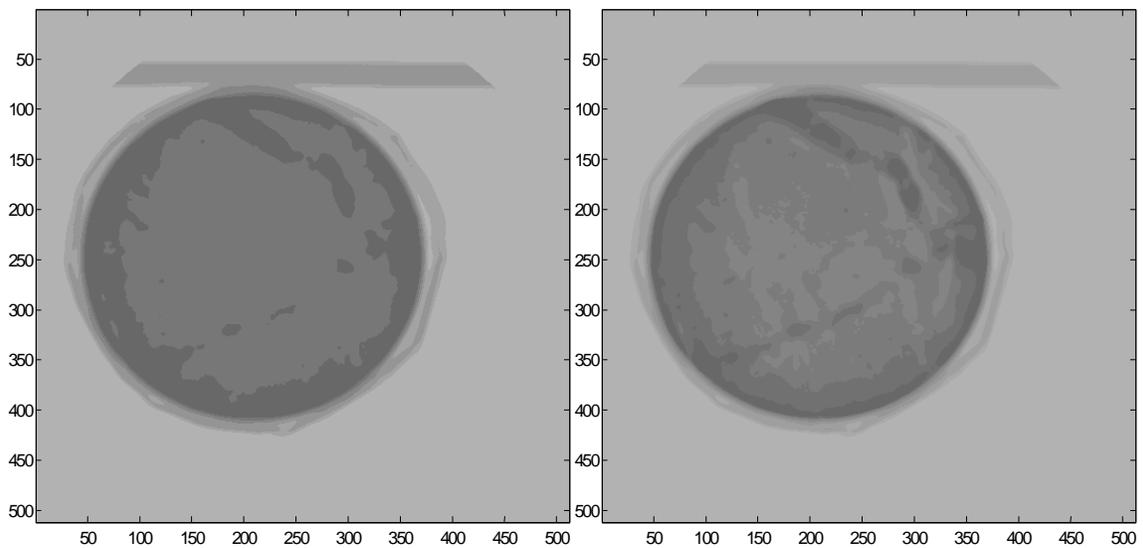


*Figure 4.4: Left: five-region segmentation. Right: nine-region segmentation.*

## 4.3 FUTURE WORK

The next stage of the project will consider four steps:

[1] Use calibrated data to derive a correlation between the integrated missing CT number over the fracture and fracture aperture.

[2] Calculate the size of fracture aperture in naturally-fractured cores based on the calibration between integrated CT number and aperture.

[3] Characterize the small apertures which may exist partially within a pixel using an interpolating wavelet transform, which can interpolate density value between the pixels.

[4] Find a more robust method for edge detection.

# 5. BOILING IN A VERTICAL FRACTURE

This experimental study of boiling in an artificial fracture is being conducted by Research Assistant Bob DuTeaux, Dr. Cengiz Satik and Prof. Roland Horne, with the goal of understanding the propagation of a thermal front in a fracture where the liquid injectate flashes to steam. Laboratory work is described, considerations for the analysis of liquid-vapor phase change and heat transfer are outlined, and a strategy for modeling boiling in a discrete fracture has been developed. This strategy involves comparing existing empirical functions relating heat flux and excess temperature with experiments being conducted at Stanford. If these functions that describe boiling convection coefficients prove useful, a numerical model that balances the heat conduction from an impermeable rock with the advecting fluid enthalpy will be constructed. This modeling approach is justified by analytic studies that show the time constant for fluid-matrix thermal equilibrium can be much larger than the fluid residence time, and that fracture geometry can have a significant effect on the propagation of a thermal front.

## 5.1 INTRODUCTION

Fluid injected into geothermal reservoirs travels across a length scale defined by the separation between wells and on a time scale described by the residence time and arrival of an injected tracer at a production well. The characteristic time and length scales for heat transfer in a fractured reservoir with an impermeable matrix are coupled by the thermal diffusivity of rock. If the time required for heat to diffuse to the midpoint between flowing fractures is less than the tracer residence time, a relatively uniform thermal front will propagate through a fractured volume outward from the injection well. If, however, the time required for thermal diffusion between fractures is much greater than the tracer residence time, colder fluid will "finger" down the fracture surfaces toward a production well leaving great quantities of energy in place.

Several significant works analyzing heat transfer and the propagation of a thermal front in fractured media have been published (for example see Gringarten, Witherspoon, and Ohnishi, 1975, Bodvarsson, and Tsang, 1982, Pruess, 1983). These studies accurately reveal the important relationships between flow rates, thermal diffusion times, and characteristic length dimensions, however, the thermal front associated with fluid boiling in discrete fractures remains a relatively unexplored topic of research.

## 5.2 LABORATORY EXPERIMENTS

The experimental apparatus illustrated in Figure 5.1 was constructed to measure the temperatures of heat exchanged between an impermeable core and water flowing upward and boiling in the concentric annulus surrounding the core. The annulus between these two large diameter glass tubes creates an artificial fracture about 1.5 mm wide. In reality the core is a 135 mm diameter glass cylinder, closed at the bottom to hold sand that has been heated to a temperature of about 150 $^{\circ}$C. These materials were chosen because their thermal conductivity and heat capacity are similar to real rock, and this would allow the phenomena to occur on realistic time and length scales. The glass surface, unfortunately, does not have a roughness like the surface of fractured rock, so a thin film of roughened

Teflon was applied to the outside of the cylinder in later experiments to provide sites for the nucleation of bubbles. With the Teflon on the outside of the core the annulus width was much less than 1 mm.

The apparatus is about two feet tall with thermocouples attached to the inside and outside of the core. Heat flux sensors were also attached to the outside of the core. Another concentric cylinder surrounds the artificial fracture to insulate radially by applying a vacuum. In a typical experiment, water is injected near atmospheric pressure from the bottom at a slow rate, so that (without boiling) it would take a few minutes to reach the top.
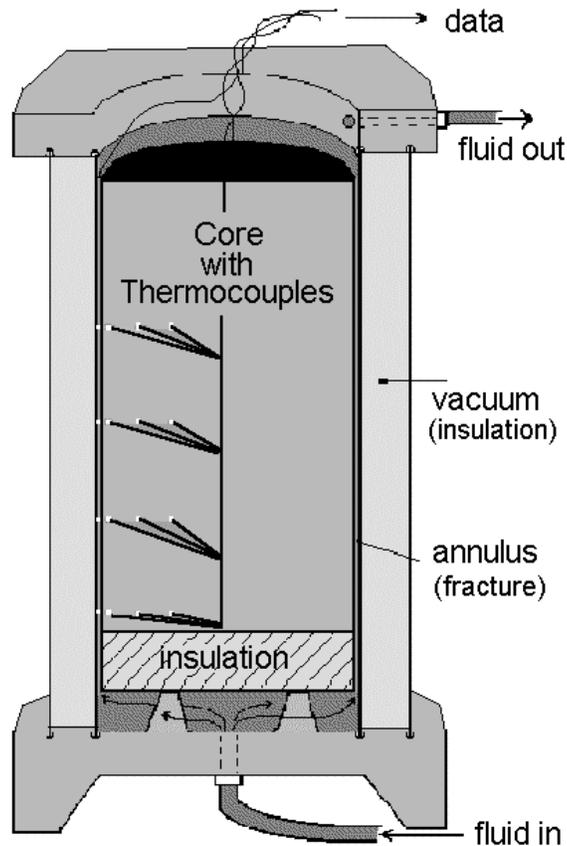


*Fig. 5.1. Illustration of experimental apparatus.*

Initially it was difficult to place thermocouples in the fluid annulus, therefore temperature measurements inside and on the surface of the heated core were recorded. Figure 5.2 shows the decline in temperature of a point on the surface of the fracture (the outer surface of the glass tube). The plot shows how the temperature changed quickly during the initial contact with fluid past the thermocouple position. Cyclic temperature fluctuations appear just after fluid contact with the thermocouple position, then a fairly rapid temperature decline occurs as water boils at that location.

The two-phase zone quickly grew to the full height of the apparatus during the experiment. With a larger aperture fracture (without the Teflon coating) the two-phase seemed to be smaller, so it is likely that the aperture has a strong influence on the extent of the two-phase region. Only a much larger apparatus, however, could confirm this.

Figure 5.2 also shows some irregular temperature inflections as boiling proceeds until boiling stopped at just above the saturation temperature. These step-like inflections have been identified in other previous experiments but have not been interpreted.
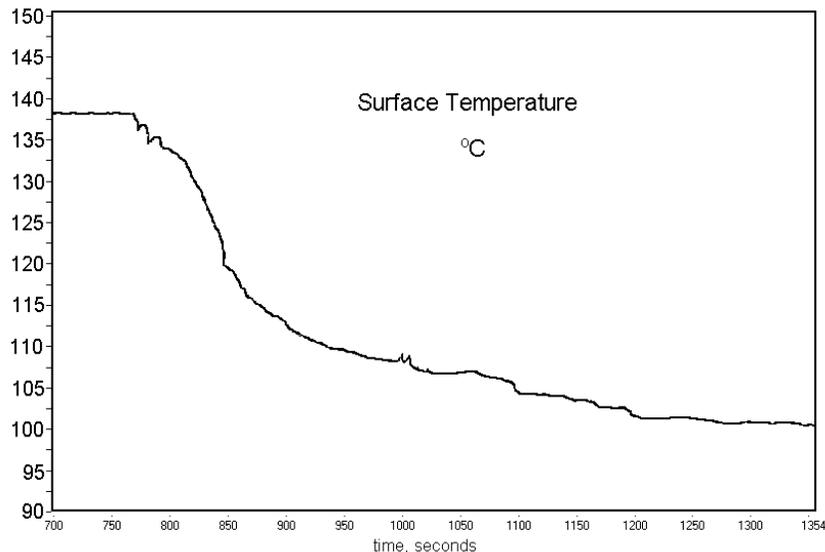


*Fig. 5.2. Surface temperature decline during boiling.*

Figure 5.3 shows the heat flux measured at two vertical locations separated by 5 cm on the core. The instantaneous maximum heat flux occurred when fluid first reached each location and then declined as boiling proceeded. The magnitude of the measured heat flux was about 6000 $W/m^2$, but this lasted only a few seconds.

Only a few experiments have been conducted to date and the data obtained has been limited. Many difficulties have been resolved and operation in the near future should provide the information needed for comparison to the work of others and for comparison to numerical simulation.

## 5.3 NUCLEATION AND EXCESS TEMPERATURE

Excess temperature, ($\Delta T_e$), defined as $\Delta T_e = T_{surface} - T_{saturation}$, is required for the nucleation of bubbles in a boiling process. However, the surface tension of a fluid and the size distribution of small asperities (and their geometry) on a fracture surface influences the $\Delta T_e$ required for nucleation. For example, very smooth surfaces require large excess temperatures because the radii of curvature of bubbles begin infinitely small and require

very large pressure differences between the vapor and the liquid to expand the bubbles. On rough surfaces, bubbles may expand more easily because they begin in the sharp crevices and expand with larger radii of curvature.  This suggests that the boiling process begins with physical dynamics that are specific to the fluid and the fracture surface involved.  Therefore, laboratory measurements derived from fluids and surfaces unlike geothermal fluids and real rocks may not provide accurate parameters for modeling real reservoir fractures.
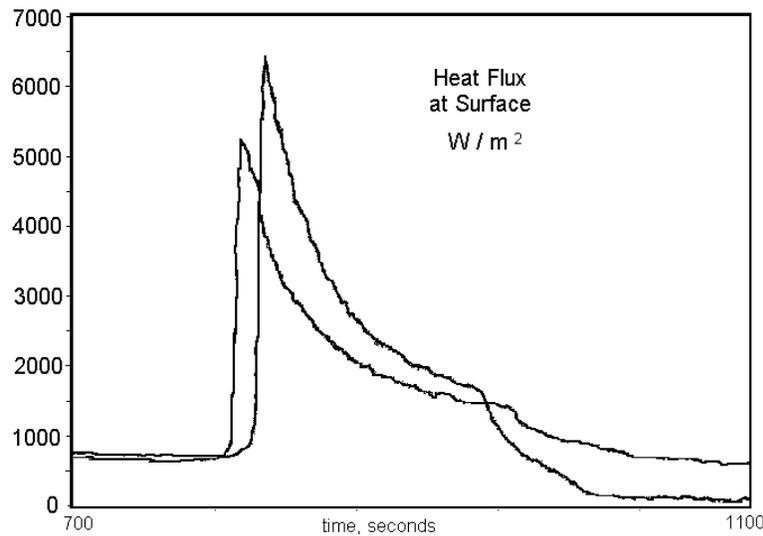


*Fig. 5.3.  Heat flux measurements during boiling.*

Although no rigorous theory exists, it is generally accepted that departing bubbles promote the mixing of a superheated boundary layer with the bulk fluid, and the bulk fluid displaces the volume previously occupied by the bubble bringing cooler fluid into contact with the surface.  On a small scale, surface temperature fluctuations occur that can not be resolved by macroscopic models. In a small fracture, the dimension of the aperture will affect bubble expansion and vapor mobility, therefore the relative permeability of liquid and vapor as a function fracture aperture size may be important for characterizing boiling in fractures.

## 5.4 BACKGROUND ON BOILING HEAT TRANSFER

The small thermal diffusivity of rock restricts the quantity of heat that can quickly conduct to a fluid boiling at a fracture surface.  This means that large temperature gradients (and transiently large heat fluxes) develop near flowing fractures.

Fluid properties, as well as rock properties, govern the advection of heat with a fluid in a boiling fracture.  Surface tension ($\sigma$), the latent heat of vaporization ($h_{fg}$), viscosity ($\mu$), flow velocity ($u$), fluid conductivity ($k$), the liquid and vapor phase heat capacities ($C_{p,liq/vap}$), and the density difference between the liquid and vapor ($\rho_{liq}-\rho_{vap}$), gravity g, and length dimension L, are fundamental parameters.  In order to reduce the number of functional variables to a minimum these may be grouped into a smaller number of

35

dimensionless groups. The common groups relevant for boiling include the Reynolds number $\rho\, u\, L\, /\, \mu$ (Re), the Prandtl number $\mu\, Cp\, /\, k$ (Pr), the Jakob number $C_p\, \Delta T_e\, /\, h_{fg}$ (Ja), and the Bond number $g\, (\rho_{liq}-\rho_{vap})\, /\, \sigma$ (Bo). The Nusselt number $h\, L\, /\, k$ (Nu), which characterizes the convection coefficient h, is considered a function of the above dimensionless parameters (Incropera and DeWitt, 1990), but may also be influence by additional factors in fractured rock. For example, in fractures capillary forces and relative permeability will affect the mobility of the vapor, so the fracture aperture may have a significant influence on how vapor nucleates, expands, and moves.

Internal flow heat transfer is commonly characterized by the Nusselt number, which can be viewed as a dimensionless convection coefficient and describes the temperature gradient at the surface-fluid contact. The convection coefficient is a factor of proportionality between the heat flux and the temperature difference in accordance with Newton's law of cooling $q" = h(T_{surface} - T_{fluid})$. With boiling, the convection coefficient is a function of excess temperature, $h = q"/\Delta T_e$, and h can be 2 to 3 orders of magnitude larger for boiling than for single phase flow.

A commonly employed illustration of the relation between surface heat flux and $\Delta T_e$ is the boiling curve, shown in Figure 5.4.

This curve is specific to a particular fluid-surface combination at a particular pressure, and it describes the boiling regimes labeled: Free convection, Nucleate, Transition, and Film boiling (Carey, 1992).
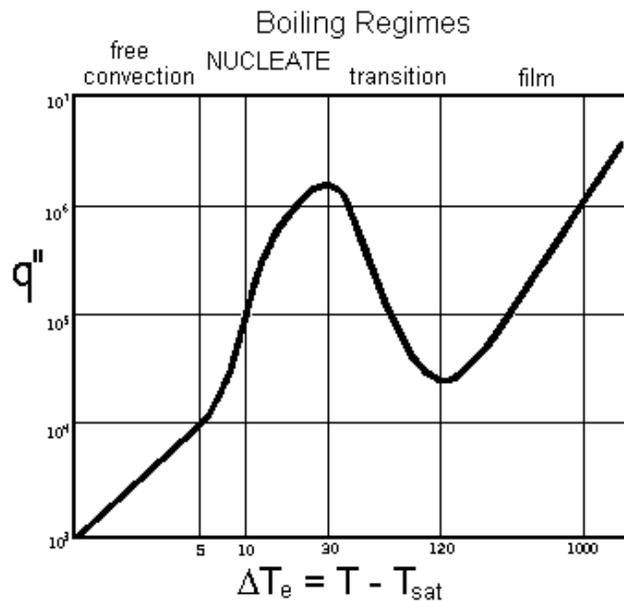
*Fig. 5.4. Boiling curve for water at 1 atm.*

Free convection occurs before the nucleation of bubbles and extends into temperatures slightly above the saturation temperature. Vapor bubbles form in the nucleate region. The nucleate region of the boiling curve describes an increasing surface heat flux with $\Delta T_e$ until a the boiling heat flux reaches a maximum. The maximum occurs because the vapor covers an increasing fraction of the surface area and restricts heat flow due to its smaller thermal conductivity and heat capacity. In the Transition Regime vapor covers an increasing fraction of the total surface area and further reduces heat flux with $\Delta T_e$. At the local minimum between the Transition and Film regimes vapor completely covers the surface. With increasing $\Delta T_e$ in the Film Regime q" increases much more slowly than in the Nucleate Regime. (Notice the scale in the Film Regime).

Empirical studies of boiling quantify either the heat flux at the surface or the convection coefficient as functionally dependent upon the aforementioned parameters and the $\Delta T_e$. One well known example of an empirical relation, valid in the nucleate boiling regime, was developed by Rohsenow in 1952, with q" = $(\mu_{liq} h_{fg}) [g(\rho_{liq}-\rho_{vap})/\sigma]^{0.5} \{C_{p,liq} \Delta T_e / (C_{s,f} h_{fg} Pr^n)\}^3$, where $C_{s,f}$ and n are characteristic of the surface and fluid to be determined by experimental data. Many other similar empirical relationships have been developed by other researchers, (Lung, Latsch, and Rampf, 1977), and these descriptions of h in a functional relation provide an approach for modeling phase change in a discrete fracture. Although this kind of relationship has been extremely useful in mechanical engineering applications such as heat exchangers in refrigeration, experimental studies with real fractures and geothermal rocks have not yet been conducted. Furthermore, most of these relations were developed with unconfined surfaces in horizontal orientations. They lack the potentially important parameters such as aperture and a description of relative permeability that influence two-phase flow in fractures. Clearly, further experimental work with the realistic rock fractures and fluids would be required to establish accurate functional relationships for modeling boiling in fractured rock.

## 5.5 NUMERICAL MODEL

Because the extent of a liquid/vapor zone in a flowing fracture is likely to be a function of the aperture, inclination, and surface roughness, it is unlikely that a sharp phase boundary could be meaningfully simulated. A formulation that employs an energy balance between the rock matrix and the fluid enthalpy, however, could be constructed from the empirical functions similar to those previously described. While the heat supplied to a fracture can be modeled by a discretization of the heat diffusion equation, the energy supplied to the fluid with a convection boundary condition can modeled as a change in fluid enthalpy. This type of formulation does not require explicitly tracking the phase interface (Voller, 1997), and a thermal front could appropriately be defined in terms of fluid enthalpy.

This formulation would couple the heat transfer in the rock matrix governed by: $\rho_{rock} C_{p,rock} \delta T/\delta t = k_{rock} \delta^2 T/\delta x^2$ with heat transfer to the fluid: $\rho_{fluid} dH/dt = h \Delta T_e$. If initial laboratory studies of boiling in fractures affirms the general utility of such empirical functions, future efforts could proceed toward constructing this kind of discrete fracture geothermal model.

# 6. MODELING OF GEOTHERMAL RESERVOIRS CONSTRAINED TO INJECTION RETURN DATA

This project is being conducted by Research Assistant Ma. Michelle Sullera and Prof. Roland Horne. It aims to deduce injection return mechanism(s) and flow paths from correlations between producer chloride concentration and injection operating parameters (flow rate and injection chloride).

## 6.1 COMPARING DATA SETS

This project was motivated by observations made on chloride and injection data from Palinpinon. The texture of the Palinpinon data set is such that the superimposed variations in chloride concentration due to well interference effects are easily distinguished from the underlying natural increasing trend with time (Fig. 6.1) Specifically, a production well's response to changes in another well's injection rate is readily inferred from coinciding peaks in the chloride concentration and injection rate. This rich texture of the Palinpinon data set makes linear regression more suitable for distinguishing between the different levels of contribution from injection wells. On the other hand, the Dixie Valley data set does not display much texture; the increasing trend of chloride concentration with time dominates the production well behavior and response to changes in injection rates is not readily evident (Fig. 6.2) This explains the very low values of linear coefficients of injection rates obtained from regression analysis of Dixie Valley data set. For Dixie Valley, injection rate coefficients are less than 0.005% of time coefficient; whereas, for Palinpinon injection rate coefficients are approximately 4% of time coefficients.

## 6.2 NUMERICAL MODELING

Results of the earlier linear correlation work were incorporated in a multicomponent (water and chloride) numerical model of the Dixie Valley reservoir. A 34x13 two-dimensional grid with single-porosity blocks was used to model the field (Fig. 6.3). In the model, fluid produced from the wells is passed on to a separator; and, brine from the separator is divided among the injection wells. The degree of connectivity between producers and injectors deduced from the linear correlation was modeled by varying the permeability of blocks between these wells. However, software problems were encountered during this numerical modeling phase. The version of the simulation software we used could not reproduce the nonpartitioning property of salt; that is, the software allowed the salt to 'evaporate' with the steam thus preventing us from modeling the increase in concentration of chloride in the reservoir with time.

Meanwhile, we have acquired a third set of data from Tiwi geothermal field on which we will perform the same analysis done on the Palinpinon and Dixie Valley data set. A more recent version of the simulator TETRAD will be used for numerical modeling of both this third chloride data set and the Dixie Valley data set.
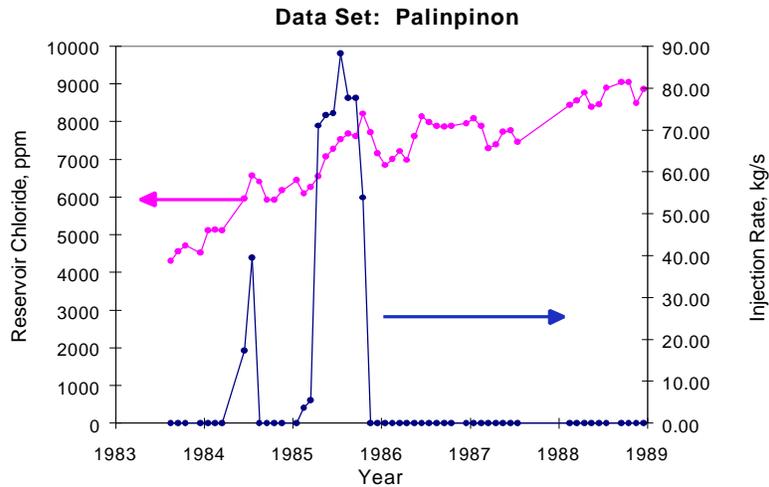
*Fig. 6.1. Chloride and injection data from Palinpinon.*
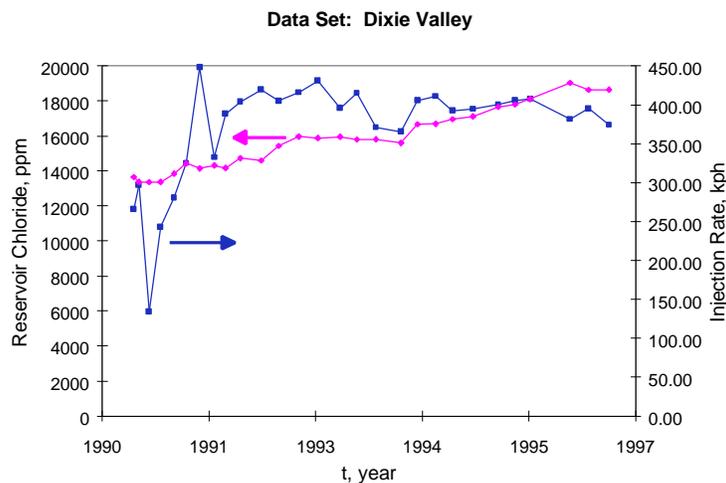


*Fig. 6.2. Chloride and injection data from Dixie Valley*

### 6.3 NEW TOOL:  WAVELET ANALYSIS

Recent use of wavelet analysis in analyzing production data from oil fields prompted us to look into its applicability to this project.  A discussion of the theory of wavelet analysis was provided in Section 4 of this report.  The same principle used by Jansen and Kelkar (1997) in inferring interwell relationships based on wavelet decomposition of injection and production rate data may be applied to our chloride-injection rate data set.  Wavelet transformation is used to decompose the data to a combination of frequency and smoothed components.  Correlation between high frequency components of the data are then inferred at different times;  thus, making the time dependent nature of the correlation evident.  To be able to extend Jansen's approach to our problem however, the amount of data at hand should be such that it could be decomposed to a number of frequencies enough to form a linear correlation between chloride concentration and injection rates at

any time.  Each of the data sets will be checked for sufficiency for this analysis.  If data is not sufficient for multiple well correlation, two-well correlation will be performed.
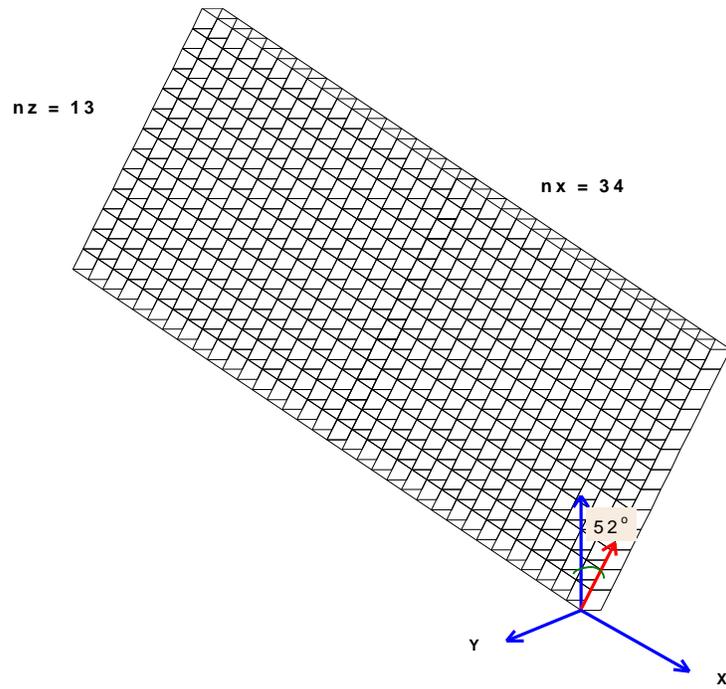


*Fig. 6.3.  Simulation grid for Dixie Valley reservoir model.*

# 7. MODELING STEAM-WATER RELATIVE PERMEABILITY

This new research project is being initiated this quarter by Research Assistant Glenn Mahiya and Professor Roland Horne. The aim of this project is to understand the fundamental physics of relative permeability of steam and water in porous media, in order to better understand the results being generated in the experimental programs (Sections 1 and 3).

## 7.1 INTRODUCTION

Steam-water relative permeability impacts the ability to forecast reservoir performance of geothermal systems. This, however, is still not clearly understood despite experiments leading to empirical correlations. Moreover, such analytic representations obtained from data-fitting are applicable only to the specific core used in the experiments. The challenges associated with conducting relative permeability measurements have hindered the reproducibility of results that will aid in understanding the factors influencing this phenomenon. The recent refinements in the experimental setup (Section 1 of this report) are expected to facilitate further efforts to obtain relative permeability curves.

## 7.2 FUTURE WORK

As a starting point, the fundamentals of steam and water retention and flow in porous media will be reviewed. Understanding the physics of mass as well as energy transport at the pore scale is essential before experiments can be designed to investigate the effect of parameters that most significantly affect relative permeability. The analysis will then be extended to ideal configurations of porous material such as a collection of capillary tubes or a network of pores. The latter approach may be pursued through numerical simulation. Once the parameters on which relative permeability strongly depends are identified from the analyses, laboratory experiments may then be set up to confirm or refute the theoretical predictions. The results of the most recent experiments to measure steam and water relative permeabilities will be analyzed to gain additional insights on steam and water flow in porous media, and a conceptual model that can reproduce the results will be constructed.

# 8. REFERENCES

Ambusso, W.J., 1996. Experimental Determination of Steam-Water Relative Permeability Relations. MS Thesis, Stanford University, Stanford. CA.

Ambusso, W.J., Satik C. and Horne, R.N., 1996. A Study of Relative Permeability For Steam-Water Flow in Porous Media. Proc. of 21st on Stanford Workshop on Geothermal Reservoir Engineering.

Arihara, N., 1976. A Study of Non-Isothermal Single and Two-Phase Flow Through Consolidated Sandstones, PhD dissertation, Stanford University, Stanford, CA.

Bodvarsson, G. S., and C. F. Tsang, "*Injection and Thermal Breakthrough in Fractured Geothermal Reservoirs*", J. Geophysical Research, vol. 87, no. B2, pgs. 1031-1048, Feb. 1982

Brooks R.H. and Corey, A.T., 1964. Hydraulic Properties of Porous Media, Colorado State University, Hydro paper No.5.

Carey, V. P., *Liquid-Vapor Phase Change Phenomena:  An Introduction to the Thermophysics of Vaporization and Condensation Processes in Heat Transfer Equipment.*  Washington, D. C.:  Hemisphere Publishing Corp., 1992.

Chen, H.K., 1976.  Measurement of Water Content in Porous Media Under Geothermal Fluid Flow Conditions. Ph. D. Thesis, Stanford University, Stanford, California

Chen, H.K., Council J.R. and Ramey, H.J., Jr., 1978. Experimental Steam-Water Permeability Curves. GRC Trans. Vol. 2 pp 102-104.

Clossman, P.J. and Vinegar, H.J., 1988. Relative Permeability to Steam and Water at Residual Oil in Natural Cores; CT Scan Saturation. SPE Paper 17449.

Corey, A.T., 1954. The Interrelations Between Gas and Oil Relative Permeabilities, Producers Monthly Vol. 19 pp 38-41.

Counsil, J.R., 1979. Steam-Water Relative Permeability. Ph. D. Thesis, Stanford University, Stanford, California.

Finsterle, S., Pruess, K. and Fraser, P., 1996. ITOUGH2 Software Qualification.

Finsterle, S., 1997. ITOUGH2 Command References Version 3.1.

Grant, M.A., 1977. Permeability Reduction Factors at Wairakei, Presented at AIChE-ASME Heat Transfer Conference, AIChE, Salt Lake City, Utah, August pp 15-17.

Gringarten, A. C., P. A. Witherspoon, and Y. Ohnishi, "*Theory of Heat Extraction from Fractured Hot Dry Rock*", J. Geophysical Research, vol. 90, no. 8, March, 1975.

Hassler, G.L., 1944. Method and apparatus for permeability measurements. U.S. Pat. Off., Washington, D.C., 1944.

Horne R.N. and Ramey, H.J., Jr., 1978. Steam/Water Relative Permeabilities From Production Data, GRC Trans. Vol. 2 pp 291.

Incropera, F. P., and DeWitt, D. P., *Fundamentals of Heat and Mass Transfer, 3$^{rd}$ Edition*. New York:  John Wiley & Sons, 1990.

Jansen, F.E. and Kelkar, M.G., 1997, "Application of Wavelets to Production Data in Describing Inter-Well Relationships", paper SPE 38876, presented at 1997 SPE Annual Technical Conference and Exhibition.

Lung, H., K. Latsch, and H. Rampf, "*Boiling Heat Transfer to Subcooled Water in Turbulent Annular Flow"*  In Hahne, E. and Grigull, U. (eds.) Heat Transfer in Boiling, Hemisphere Publishing, 1997, pp. 220.

Ma S. and Morrow, N.R., 1991. Effect of Firing on Petrophysical properties of Berea Sandstone, SPE Paper 21045, Presented at SPE International Symposium on Oilfield Chemistry, Anaheim, CA, Feb. 20-22.

Miller, F.G., 1951. Steady Flow of Two-Phase Single-Component Fluids Through Porous Media, Trans. AIME, 192, 205.

Osoba, J.S., Richardson, J.J., Kerver, J.K., Hafford, J.A. and P.M. Blair, P.M., 1951. Laboratory Measurements of Relative Permeability. Transactions, AIME, Vol.192, pp 47-55.

Piquemal, J., 1994. Saturated Steam Relative Permeabilities of Unconsolidated Porous Media. Transport in Porous Media 17, pp 105-120.

Pratt, W.K., 1991, "Digital Image Processing", John Wiley & Sons, Inc.

Pruess, K., 1987. TOUGH User's Guide.

Pruess, K., 1991. TOUGH2-A General Purpose Numerical Simulator for Multiphase Fluid and Heat Flow.

Pruess, K., "*Heat Transfer in Fractured Geothermal Reservoirs with Boiling*", Water Resources Res., 19, 201-208, 1983.

Rohsenow, W. M., *"A Method of Correlating Heat Transfer Data for Surface Boiling Liquids, Trans,"* ASME, 74, 969-975, 1952.

Sanchez, J.M., 1987. Surfactant Effects on the Two-Phase Flow of Steam/Water and Nitrogen/Water in an Unconsolidated Permeable Medium. Ph. D. Thesis, University of Texas, Austin, Texas.

Satik, C., Ambusso, W.J., Castanier, L.M. and. Horne, R.N., 1995. A Preliminary Study of Relative Permeability in Geothermal Rocks, GRC Trans. Vol. 19, pp 539.

Satik, C., 1998. A Measurement of Steam-Water Relative Permeability, Proc. of 23rd Workshop on Geothermal Reservoir Engineering.

Sorey, M.L. Grant, M.A. and Bradford, E., 1980. Nonlinear Effects in Two Phase Flow to Wells in Geothermal Reservoirs. Water Resources Research, Vol. 16 No. 4, pp 767-777.

Verma, M.A., 1986. Effects of Phase Transformation of Steam-Water Two-Phase Relative-Permeability. Ph.D. Thesis. University of California, Berkeley.

Voller, V. R., "*An Overview of Numerical Methods for Solving Phase Change Problems."* in Minkowycz, W. J. and Sparrow, E. M. (eds.) Advances in Numerical Heat Transfer, Washington, DC: Taylor and Francis, 1997, pp. 341-375.